
Ocean currents and gradients of surface layer properties in the vicinity of the Madagascar Ridge (including seamounts) in the South West Indian Ocean

Vianello Patrick ¹, Ternon Jean-Francois ², Demarcq Herve ², Herbette Steven ³, Roberts Michael J. ^{1, 4, *}

¹ UK-SA NRF/DST Bilateral Research Chair: Ocean Sciences and Marine Food Security, Nelson Mandela University, Port Elizabeth, South Africa

² MARBEC, IRD, Univ Montpellier, CNRS, Ifremer, Sète, France

³ Laboratoire d'Océanographie Physique et Spatiale (LOPS), IUEM, Univ. Brest - CNRS - IRD - Ifremer, Brest, France

⁴ National Oceanography Centre, Southampton, United Kingdom

* Corresponding author : Michael J. Roberts, email address : mike.roberts@mandela.ac.za

Abstract :

This work is part of the MADRidge Project special issue which aims to describe pelagic ecosystems in the vicinity of three prominent shallow seamounts in the South West Indian Ocean: one here named MAD-Ridge (240 m below the surface) plus Walters Shoal (18 m) on the Madagascar Ridge, and La Pérouse (60 m) on the abyssal plain east of Madagascar. The three span latitudes 20°S and 33°S, some 1500 km. The study provides the background oceanography for the once-off, multidisciplinary snapshot cruise studies around the seamounts. As life on seamounts is determined by factors such as summit depth, proximity to the light layers of the ocean, and the ambient circulation, a first description of regional spatial-field climatologies (16–22 years) and monthly along-ridge gradients of surface wind (driving force), water column properties of sea surface temperature, mixed layer depth, chlorophyll-a and eddy kinetic energy, plus ocean currents is provided. Being relevant to many applications in the study domain, these properties in particular reveal contrasting environments along the Madagascar Ridge and between the three seamounts that should drive biological differences. Relative to the other two seamounts, MAD-Ridge is in the more extreme situation, being at the end of the East Madagascar Current, where it experiences sturdy, albeit variable, currents and the frequent passing of mesoscale eddies.

Keywords : South West Indian Ocean, Madagascar Ridge, Seamounts, Walters shoal, Sea surface temperature, Eddy kinetic energy, Mixed layer depth, Chlorophyll-a, Geostrophic currents

39

40 1. Introduction

41

42 1.1. Importance of ridges and seamounts

43 Most of the world's extensive seafloor consists of a deep muddy plain inhabited by molluscs,
44 worms and echinoderms (Thistle, 2003). Bathypelagic fish are few. It is only sharp ridges and
45 seamounts that provide a deep-sea relief, rocky and sediment-free, that can support abundant
46 diverse and distinctive fauna. Seamounts are of volcanic origin, and tend to be on the oceanic
47 crust near mid-ocean ridges, mantle plumes (hotspots) and island arcs (Keating et al., 1987).
48 They range from isolated landmarks to clusters and chains (Roberts et al., 2020). Estimates of
49 the number of seamounts in the global ocean vary between 10 000 and 100 000 (Kitchingman
50 et al., 2007; Harris et al., 2014). The total area of these features is equivalent to about 30% of
51 the global shelf region, making them significant platforms in sustaining life in the vast, deep
52 ocean. With structure for animals to settle and live on, and currents supplying nutrients and
53 food, the variety of life at seamounts is often great. This situation has been noticed by fishers
54 who, in many cases, have plundered species of commercial value such as the deep-living
55 orange roughy (*Hoplostethus atlanticus*) and Patagonian toothfish (*Dissostichus eleginoides*)
56 at the base of seamounts, and various tuna species and swordfish around the summits.

57

58 However, given the large number of seamounts globally and their remote locations, much
59 about the structure, function and connectivity of seamount ecosystems remains unexplored
60 and unknown. Threats such as fishing and seabed mining are creating an unprecedented
61 demand for research to inform conservation and management strategies. Clark et al. (2012) in
62 particular called for renewed and intensive scientific effort to enhance the physical and
63 biological information on seamount location, physical characteristics, comprehensiveness of
64 biodiversity inventories, and the understanding of seamount connectivity and faunal
65 dispersal.

66

67 1.2. What shapes life on seamounts?

68 Most seamounts lie deep beneath the ocean surface, rising <1 500 m from the abyssal plains.
69 A few reach the photic zone, and even fewer protrude above the ocean surface to form
70 islands. Their volcanic nature and steep sides mean that bottom sediment loads tend to be
71 low, providing islands of exposed hard substratum in the wider ocean. However, there are
72 also other factors that determine the nature of the benthic and pelagic ecosystems that evolve

73 around seamounts. Shape and summit depth determine the interactions with the surrounding
74 oceanography, especially currents. Current velocities are strongest at the surface but decrease
75 rapidly with depth. A protruding seamount disturbs the water flow, causing eddies of varying
76 size (sub-mesoscale to mesoscale), internal waves, turbulent mixing and upwelling. A
77 specific seamount-associated eddy is known as a Taylor column (or sometimes Taylor cap),
78 which is anticyclonic and stationary over the summit, and it tends to retain small particles
79 such as plankton and larvae. Such physical processes induce vertical movement of deeper,
80 nutrient-rich water towards the sea surface which, given sufficient light, can enhance local
81 plankton populations, and result in seamounts being aggregation areas for micronekton
82 feeding (Lavelle and Mohn, 2010). The small fish in turn fall prey to predation by
83 cephalopods, tuna, sharks and marine mammals, plus seabirds when the features are notably
84 shallow. Other factors including water temperature, the depth of the upper mixed layer (and
85 wind) and the extent of stratification, all play a role in shaping the benthic and pelagic
86 ecosystems around seamounts.

87

88 The clear water conditions in the open ocean allow photosynthesis at greater depths than
89 around continental shelves, so coralline algae for example can live at depths of 270 m (Littler
90 et al., 1986). However, as depth increases beneath the upper sunlit layers of the ocean, current
91 velocities and temperatures decrease, creating a different environment for the benthos.
92 Evolving over millions of years, seamounts seem to have become isolated habitats that
93 support communities high in endemism (Rogers, 1994; Tyler et al., 1995; Parin et al., 1997;
94 Richer de Forges et al., 2000). Their isolated benthic and pelagic ecosystems make seamounts
95 biological hotspots, stopping points for migrating animals such as whales, and stepping
96 stones for the dispersion of biota across ocean basins. The position of a seamount relative to
97 current systems, landmasses and latitude will influence dispersion, connectivity and ambient
98 water properties.

99

100 *1.3. Ridges and seamounts in the South West Indian Ocean*

101 As stated by Roberts et al. (2020), most seamounts in the Indian Ocean are on the western
102 side of the basin, notably along the South West Indian Ridge (SWIR). Fishers for decades
103 have explored and fished the numerous seamounts on this ridge, first Soviet fleets, then
104 French and Asian fleets in the 1970s and 1980s (Clark et al., 2007; Rogers et al., 2017). More
105 recently, since 1990, the tuna longline fishery, mostly working from Réunion Island (Evano

106 and Bourjea, 2012), has focused on a region south and east of Madagascar, where
107 productivity seems to be enriched, a statement supported by studies on seabirds (Pinet et al.,
108 2012). The region south of Madagascar overlies the Madagascar Ridge, an impressive
109 bathymetric feature that to date has received little scientific attention because of its
110 remoteness.

111

112 Aligned longitudinally, the Madagascar Ridge extends south of the Madagascar landmass for
113 some 1 300 km (~10 degrees of latitude; **Fig. 1** and **2**) with a width of ~400 km. Water depths
114 over much of the ridge are between 2 and 3 km. The southern half of the ridge rises to the
115 prominent Walters Shoal, one of a group of several deeper seamounts, but which itself comes
116 within 18 m of the surface (**Fig. 2b**). Its flat summit is covered by coral reef, with broken and
117 jagged relief, especially along the outer edges. The northern part of the Ridge likewise
118 consists of a cluster of seamounts shallower than 750 m. One of these, referred to in this
119 study as the MAD-Ridge seamount, rises to a depth of 240 m below the sea surface (27.5°S,
120 46.25°E; Roberts et al., 2020). The western side of the Madagascar Ridge has a steep scarp
121 that runs down into the 5-km-deep Mozambique Basin. The slope of the eastern flank is
122 gentler, leading into the 5–6-km-deep Madagascar Basin. South of Walters Shoal, the water
123 depth increases rapidly to more than 3000 m, whereupon, the 4000 m isobath joins the SWIR.
124 Even with the northern and southern seamount clusters, the ridge is mostly flat-topped and
125 covered by 0.5–1.0 km of undisturbed sediments (Goslin et al., 1980).

126

127 *1.4 Regional oceanography*

128 The Madagascar Ridge lies in a region of the southern Indian Ocean where the Subtropical
129 Anticyclonic Gyre forms the general background circulation (**Fig. 1a**; Stramma and
130 Lutjeharms, 1997; Lutjeharms., 2006), circulation portrayed by the baroclinic volume flux
131 field over the upper 1000 m. Closure of the Subtropical Gyre has not yet been completely
132 resolved (Pollard and Read, 2015). The gyre includes the powerful Agulhas Current (AC) as
133 the major western boundary current (**Fig. 1b**). This flow retroflects at the southern tip of
134 Africa, and mostly flows back east as the Agulhas Return Current (ARC), undergoing a series
135 of semi-permanent meanders between 37°S and 41°S just north of the Subtropical Front
136 (STF). The ARC weakens towards the east as transport peels off to the north (Stramma and
137 Lutjeharms, 1997; Lutjeharms, 2007), then turns west to close the anticyclonic gyre.
138 Northward leakage from the ARC also occurs in the form of cyclonic eddies that regularly

139 form and break away, moving west (Pollard and Read, 2015). The westward recirculation
140 within the Southwest Indian subgyre flows across the Madagascar Ridge.

141

142 The circulation south of Madagascar is complex and dominated by the strong South East
143 Madagascar Current (S-EMC; Nauw et al., 2008). Similar to the situation for the AC,
144 Lutjeharms (2007) suggested that the S-EMC undergoes an eastward retroflexion once it
145 becomes a free jet south of the landmass. Mesoscale eddies are formed there, which then
146 propagate west towards southern Africa, where they merge with the upper reaches of the AC
147 (Halo et al., 2014; Braby et al., 2016; de Ruijter et al., 2004). Ridderinkhof et al. (2013)
148 demonstrated that much of this propagating turbulence is in the form of dipoles. Quartly et al.
149 (2006) suggested that the retroflexion at the end of the S-EMC is not a permanent feature.
150 Siedler et al. (2006, 2009), on the basis of climatological altimetry data, proposed that the
151 South Indian Ocean Countercurrent (SICC) was an eastward extension of the S-EMC
152 retroflexion. Palastanga et al. (2007) observed the SICC to extend to 100°E, and Siedler et al.
153 (2009) suggested that up to 40% of SICC waters originate in the S-EMC.

154

155 Not much is known of the circulation south of the S-EMC retroflexion area. Read and
156 Pollard (2017) suggested that integrated westward transport between Madagascar and 37°S
157 accounts for 50 Sv, which added to 25 Sv from the S-EMC, is sufficient to account for the
158 total AC transport of 70 ± 21 Sv, i.e. that it is a slow background flow. Observations from
159 altimetry data show, superimposed on this background, that the southern part of the
160 Madagascar Ridge is regularly affected by low-intensity eddies that propagate westwards
161 (Read and Pollard, 2017).

162

163 *1.5 Aims of this paper*

164 The MADRidge Project (Roberts et al., 2020) was established in 2016/17 to further
165 understanding of the pelagic ecosystems potentially supporting the productivity over the
166 Madagascar Ridge and east of Madagascar. Three prominent shallow seamounts were
167 selected for scientific investigation: two on the Madagascar Ridge, the Walters Shoal (18 m
168 below the surface) and MAD-Ridge (240 m), and one east of Madagascar, La Pérouse (60 m),
169 which rises from the abyssal plain. With the wish to help answer the question as to what
170 shapes life on seamounts (see above), the present study was designed to provide a regional
171 view of surface wind as a driver of upwelling and mixing, sea surface temperature (SST),
172 mixed layer depth (MLD), and chlorophyll-*a* (hereafter chl-*a*) as key water column

173 properties, and eddy kinetic energy (EKE) and currents as drivers of seamount processes and
174 dispersion/connectivity. We attempt to provide a backdrop to the more-detailed ship-based,
175 satellite and modelling investigations that supplement this study in the MADRidge Project
176 special issue.

177

178 **2. Data and methods**

179

180 *2.1 Study area and bathymetry*

181 The GEBCO 2014 gridded bathymetry product
182 (https://www.gebco.net/data_and_products/gridded_bathymetry_data/) was used to display the
183 bathymetry of the Madagascar Ridge, the two prominent seamounts Walters Shoal and
184 MAD-Ridge, and the broader surroundings in the region, shown in **Fig. 1** and **2**). The product
185 consists of a global terrain model for ocean and land at 30 arc-second intervals. Actual depths
186 for the three prominent seamounts (including La Pérouse) were obtained from cruise surveys
187 (see Roberts et al., 2020, for further detail).

188

189 *2.2 Virtual moorings*

190 As shown in **Fig. 2**, seven (numbered 1–7) ‘virtual mooring’ (VM) deployment points were
191 selected along the Madagascar Ridge to investigate the circulation dynamics along it,
192 including the MAD-Ridge seamount (VM 2) and the Walters Shoal (VM 6). At each location,
193 time-series of absolute geostrophic velocity based on altimetry data were extracted (grid
194 point) for four years (2011–2014). Position and depths at each VM position 1–7 are: VM 1
195 (46.25°E, 26.5°S; 1820 m), VM 2 (46.25°E, 27.5°S; 236 m), VM 3 (46.25°E, 28.5°S; 3170
196 m), VM 4 (45.63°E, 30.38°S; 2520 m), VM 5 (44°E 32.25°S; 1200 m), VM 6 (44°E,
197 33.25°S; 18 m) and VM 7 (44°E, 34.25°S; 2330 m). The altimetry data described below were
198 used to calculate current vectors for each position every four days over the period 2011–
199 2014.

200

201 *2.3 Altimetry data*

202 Merged, daily interpolated, delayed time (DT), altimetry data gridded at $\frac{1}{4}^\circ$ resolution were
203 used (1993–2016). This product is produced by Ssalto/Duacs and is distributed by
204 Copernicus Marine Environment Monitoring Service (CMEMS)
205 (<http://marine.copernicus.eu/>). Mean absolute dynamic topography (MADT) data are used to
206 highlight the circulation dynamics using climatologies over the Madagascar Ridge. Mean

207 EKE is derived from the MADT data over a specified domain in the South West Indian
208 Ocean (SWIO) that includes the entire Madagascar Ridge. This is calculated using the
209 equation

$$\overline{EKE} = \frac{1}{2} (\overline{u_g'^2} + \overline{v_g'^2}),$$

210 where $\bar{}$ implies a time-average over the period 1993–2016, and $u_g'^2$ and $v_g'^2$ are the zonal and
211 meridional components of the surface total geostrophic current computed directly from the
212 MADT. The MADT data are also used to calculate the absolute geostrophic velocity at each
213 of the seven VM points along the Madagascar Ridge for the four years 2011–2014.

214

215 For near-surface ocean current estimates, OSCAR (Ocean Surface Currents Analyses Real-
216 time) products are deemed to be superior to satellite altimeter-derived geostrophic currents,
217 because the calculation is improved using satellite data and validation methods (for detail, see
218 <https://www.esr.org/research/oscar/oscar-surface-currents/>). With OSCAR, currents are
219 averaged over the top 30 m of the ocean, and provided on a global $\frac{1}{3}^\circ$ grid with a 5-day
220 resolution dating from 1992 to present. OSCAR is generated by Earth Space Research (ESR).
221 However, a comparison between OSCAR and MADT-derived products (Supplementary
222 material **Fig. S1**), showed only small differences in current direction and velocity at each
223 mooring, with the OSCAR product being mainly lower in velocity by an average of 7 cm s^{-1} .
224 A comparison of MADT-generated geostrophic velocities at VM 6 with passing historical *in*
225 *situ* surface drifters (Supplementary material **Fig. S2**) indicated the MADT product to be on
226 average 8 cm s^{-1} slower. On the basis of these determinations, it was decided to use the
227 MADT-derived geostrophic velocities herein. The absolute geostrophic velocities were also
228 validated over the northern Madagascar Ridge against cruise-collected S-ADCP data (see Fig.
229 3 of Vianello et al., 2020). Demarcq et al., (2020) used the same product.

230

231 2.4 Wind, SST, MLD and chlorophyll data

232 Wind data obtained from <http://www.remss.com/measurements/ccmp/> were used to produce
233 climatologies (1993–2015) with a spatial resolution of $\frac{1}{4}^\circ$ and a temporal resolution of 6 h.
234 These data are configured to represent a measurement 10 m above the ocean surface, and
235 comprise a cross-calibrated, multi-platform (CCMP) gridded product that uses a combination
236 of radiometer wind speeds, QuikSCAT and ASCAT scatterometer wind vectors, moored
237 buoy and model wind data, and is a Level 3 ocean vector wind analysis product (Atlas et al.,
238 2011).

239 SST data obtained from <http://data.remss.com/SST/daily/> were used to produce climatologies
240 (1998–2014) with a spatial resolution of 9×9 km and a temporal resolution of 1 day. This 9
241 km microwave optimally interpolated SST product combines the through-cloud capabilities
242 of the microwave data (25×25 km resolution), with the better spatial resolution (9×9 km)
243 and near-coast capability of the infrared SST data. An interpolated algorithm is implemented
244 to homogenise the resolution of the combined product.

245

246 The MLD data were downloaded from <http://www.ifremer.fr/cerweb/deboyer/mld/home.php>)
247 and used to produce climatologies (1985–2009) with a spatial resolution of 2° and a temporal
248 resolution of 1 month. The criterion used to obtain the MLD was: $MLD = \text{depth}$; where ($\theta =$
249 $\theta_{10\text{m}} \pm 0.2$ °C), according to de Boyer Montégut et al. (2004).

250

251 Chlorophyll-*a* data obtained from Hermes Globcolour (<http://hermes.acri.fr/>) were used to
252 produce climatologies (1998–2016) with a spatial resolution of 4×4 km and a temporal
253 resolution of 1 day.

254

255 3. Results

256

257 3.1 Regional climatology maps

258 3.1.1 Surface winds

259 **Fig. 3a** and **3b** show the summer (a) and winter (b) climatology (1993–2015) for the regional
260 wind field inclusive of the Madagascar Ridge. In this study, summer refers to December,
261 January and February and winter to June, July and August. Colours represent wind speed, and
262 the direction is shown by the white arrows (vectors). The black horizontal lines depict the
263 latitude of the Mad-Ridge seamount and Walters Shoal. In austral summer, the wind direction
264 is easterly along the entire Ridge (trade winds), with speeds increasing from 6.5 to 8.5 m s^{-1}
265 in the northern part. The wind field deflects around southern Madagascar, but there is also a
266 permanent local acceleration ‘hotspot’ off the southeast coast. This extends to the MAD-
267 Ridge seamount and is stronger during winter. This hotspot has also been noted by Collins et
268 al. (in prep.). During summer, the westerly wind belt is found south of 36°S and does not
269 reach the Ridge, but in winter it moves north and impinges on the southern reaches of the
270 Ridge, including the Walters Shoal (Rubin and van Loon, 1953), bringing with it stronger
271 winds of >9 m s^{-1} . Winds near La Pérouse at 20°S tend to be moderate (6 – 7 m s^{-1}) year-
272 round.

273

274 *3.1.2 Sea surface temperature*

275 The regional seasonal SST climatologies (1998–2014) for the domain that interests us here
276 are depicted in **Fig. 3c** and **3d**. Most notable in these maps is the seasonal meridional
277 movement of surface isotherms, typified by the 20 and 25°C contours (shown). There is also
278 a permanent zonal SST gradient with warmer temperatures in the west being farther south
279 than in the east, no doubt a consequence of the influence of the AC. Highest summer SSTs in
280 this regional domain, around 28–30°C, are found in the Mozambique Channel, with SSTs
281 east of Madagascar being some 2°C cooler. This zonal disparity is less during winter, when
282 SSTs cool to 24–25°C either side of Madagascar. Over the ridge, the 20°C isotherm migrates
283 south from its summer position over the MAD-Ridge seamount to the southern extreme of the
284 ridge. This implies that MAD-Ridge has a long-term average summer SST of 25.8 (± 0.7)°C,
285 which then drops in winter to 23 (± 0.9)°C. South, at the Walters Shoal, the long-term average
286 SST ranges from 21.84 (± 0.6)°C in summer to 18.4 (± 0.5)°C in winter, indicating an all-
287 round 3°C (on average) difference in surface temperature regimes. For comparison, the
288 seasonal SST range at La Pérouse is from 27.7 (± 0.8)°C in summer to 24.8 (± 0.9)°C in
289 winter.

290

291 It should be noted that the Walters Shoal is in a region where STSW (subtropical surface
292 water) dominates surface layers (Read and Pollard, 2017), whereas the MAD-Ridge
293 seamount is in an area where TSW (tropical surface water) dominates surface layers
294 (Vianello et al., 2020).

295

296 *3.1.3 Mixed layer depth*

297 The seasonal MLD climatologies (1985–2009) are shown in **Fig. 3e** and **3f**. There are large
298 seasonal differences. During summer, the MLD varies marginally with a 4-m range along the
299 Madagascar Ridge and throughout the selected domain. For example, the MLD at 30°S, 47°E
300 (white 'X') on the ridge is 23.73 (± 4.25) m. To the west (30°S, 40°E) in the Mozambique
301 Basin, it is 29.78 (± 5.38) m, and to the east on the same latitude (30°S, 51°E) it is 24.03
302 (± 4.16) m. In the far north near La Pérouse, summer MLD is 29.26 (± 7.07) m. During winter,
303 however, greater contrasts exist between north and south, ranging from nearly 120 m at 40°S
304 to 58 m near the MAD-Ridge seamount. North of there, the MLD deepens again to 84.09
305 (± 14.86) m at 20°S near La Pérouse. Note also the stark difference between the eastern side
306 of Madagascar and the Mozambique Channel, where the MLD is shallower, between 55 and

307 60 m, about the same as the northern Madagascar Ridge. The deep southern MLD values are
308 attributable to the northward migration of the westerly wind belt seen in **Fig. 3a** and **3b**.
309 Along the Ridge, the MLD deepens by some 40 m from 58.04 (± 16.7) m at 26°S, 47°E (white
310 'X') near the MAD-Ridge seamount, to 64.76 (± 13.89) m midway at 30°S, 47°E, to 99.88
311 (± 22.51) m at 34°S, 47°E in the south. Relatively, there is only a slight west–east MLD
312 gradient across the Ridge, e.g. west of the ridge at 30°S, 40°E (white 'X'), the MLD is 62.86
313 (± 15.65) m, and east of the ridge at 30°S, 51°E (another white 'X'), it is 68.60 (± 9.29) m.

314

315 *3.1.4 Eddy kinetic energy*

316 **Fig. 3g** and **3h** show the EKE climatology (1993–2016) for the Madagascar Ridge region.
317 The turbulent eddy areas (i.e. $>1000 \text{ cm}^2 \text{ s}^{-2}$) are clearly revealed, on the western side of the
318 Mozambique Channel (e.g. Roberts et al., 2014), south of the Madagascar landmass where
319 the S-EMC terminates (e.g. Siedler et al., 2009) and along the boundary of the ARC (STF)
320 near 40°S (e.g. Read and Pollard, 2017). The central region of the SWIO gyre that overlaps
321 with the southern Madagascar Ridge has the lowest EKE. Around these features, there is very
322 little difference between summer and winter regimes in terms of EKE (at least in this
323 climatological analysis). In terms of the MADRidge Project, this demonstrates that the MAD-
324 Ridge seamount and Walters Shoal are positioned in completely contrasting EKE regimes.
325 For both summer and winter, Walters Shoal has a low EKE climatology of $<50 \text{ cm}^2 \text{ s}^{-2}$,
326 whereas the MAD-Ridge seamount at the tail end of the S-EMC has a much higher EKE of
327 some $400 \text{ cm}^2 \text{ s}^{-2}$. It is worth noting that MAD-Ridge is not quite in the main high EKE
328 corridor to the north. Also, although the EKE is very low on the southern reaches of the ridge,
329 eddies are still found there, albeit infrequently and with low sea surface height (SSH) (Read
330 and Pollard, 2017). La Pérouse is situated in an area of intermediate EKE, with a mean
331 summer value of $58.9 \text{ cm}^2 \text{ s}^{-2}$ and a mean winter value of $56.9 \text{ cm}^2 \text{ s}^{-2}$.

332

333 *3.1.5 Surface chlorophyll-a*

334 The surface summer and winter chl-*a* climatology (1998–2016) are shown in **Fig. 3i** and **3j**.
335 Summer experiences low values of $\sim 0.1 \text{ mg m}^{-3}$ over much of the region. Exceptions are on
336 the southern Madagascar shelf and in the south around 35°S, where the STF is found at that
337 time of year. Note that the east Madagascar bloom, which appears at times between January
338 and April, is not evident, no doubt a consequence of its intermittent nature (Srokosz et al.,
339 2015; Dilmahamod et al., 2019). Throughout the year, the dominant high chl-*a* levels in this
340 entire region are found on the Madagascar shelf, in winter on the mid-shelf at 45.35°E, 26°S,

341 where the value is $0.24 \pm 0.07 \text{ mg m}^{-3}$. This is associated with wind-driven coastal upwelling
342 and the divergence caused at that time by the S-EMC (see also later, in **Fig. 4**). It is also
343 worth noting that there is no chl-*a* signature for the eddy corridor south of the Madagascar
344 shelf. On the Madagascar Ridge, the MAD-Ridge seamount has a climatological summer
345 mean of $0.14 \pm 0.04 \text{ mg m}^{-3}$, as does the Walters Shoal with its $0.14 \pm 0.03 \text{ mg m}^{-3}$, further
346 reinforcing the uniformity of the property. In winter, however, regional variation is apparent.
347 Little changes in the central gyre east of Madagascar, as typified near La Pérouse, with its
348 values of $0.07 \pm 0.02 \text{ mg m}^{-3}$ in summer and $0.12 \pm 0.02 \text{ mg m}^{-3}$ in winter. Chl-*a* on the
349 Madagascar shelf is higher at $0.54 \pm 0.21 \text{ mg m}^{-3}$. South of 32°S , the mean winter chl-*a*
350 begins to increase to values $>0.3 \text{ mg m}^{-3}$, the highest mean values in the entire domain for all
351 seasons. Not surprisingly, this overlaps with the deepening of the MLD shown in **Fig. 3f**, and
352 the vertical mixing of nutrients from below. The winter mean over the Walters Shoal is 0.26
353 $\pm 0.04 \text{ mg m}^{-3}$ and at MAD-Ridge $0.19 \pm 0.02 \text{ mg m}^{-3}$. The elevated chl-*a* centred around
354 33°S and west of 40°E , where values rise between 0.3 and 0.4 mg m^{-3} , presumably stems
355 from both a shallower MLD and the dynamics of the ARC. A noteworthy point too is the
356 enhanced chl-*a* west of the Madagascar Ridge, where the MLD remains deepest during
357 winter.

358

359 *3.2 Monthly water property gradients over the Madagascar Ridge*

360 As the Madagascar Ridge is the focus of the MADRidge Project, we now highlight, using
361 Hovmoller plots, the mean monthly (seasonal) dynamics of these water properties along the
362 Ridge, averaged in the area between 43 and 48°E and 26 and 40°S (see box in **Fig. 4**),
363 complementing the spatial information produced in **Fig. 3**. In the case of surface winds (**Fig.**
364 **4a**), the northward encroachment of the high velocity ($>10 \text{ m s}^{-1}$) westerly wind belt starts in
365 April, peaks in July, then subsides in October. To the north between 26 and 28°S , wind speed
366 is bimodal, with maxima of 9 m s^{-1} in February and November. These values correspond to
367 the local acceleration south of the Madagascar landmass, observed in **Fig. 3a** and **3b**, and
368 highlights the fact that the small seasonal difference seen there is an artefact of the months
369 chosen to represent summer and winter.

370

371 In the case of SST (**Fig. 4b**), a strong gradient (difference between 26 and 40°S) ranging
372 between 6 and 9°C is observed throughout the year along the Ridge. This means that at
373 Walters Shoal, SST ranges from 19°C in September to 24°C in February, and at MAD-Ridge,
374 the range is 23°C in September to 27°C in February.

375

376 As would be expected, the MLD (**Fig. 4c**) along this transect shows a similar pattern to that
377 of surface winds (**Fig. 4a**), being deeper (>100 m) south of 36°S in winter between June and
378 October. During summer, the MLD is not dissimilar (30–40 m) along the Ridge, but it is
379 deeper at Walters Shoal (i.e. 80 m) than at MAD-Ridge (55 m) in winter (July).

380

381 As already noted in **Fig. 3**, the EKE in this region is high immediately south of Madagascar
382 as a result of the S-EMC, and also south of 38°S because of the boundary dynamics of the
383 ARC. These are starkly portrayed in **Fig. 4d** too, but here we also see some intra-annual
384 variability in the EKE climatology representing the mesoscale eddy activity south of
385 Madagascar. The data highlight the period March–August as having either more eddies or
386 more-intense eddies. The EKE arising from the ARC is consistently intense and shows little
387 spatial intra-annual variability. Between these extremes, the remainder of the Madagascar
388 Ridge has low EKE throughout the year. Similar to **Fig. 3g** and **3h** this plot highlights the
389 contrasting high vs. low energy environments between MAD-Ridge and Walters Shoal (i.e.
390 low- vs. high-speed currents).

391

392 **Fig. 4e** shows low levels of chl-*a* over the Ridge, ranging from <0.1 mg m⁻³ during summer
393 to a little over 0.2 mg m⁻³ in July. Chl-*a* on the Madagascar shelf, in terms of climatology,
394 peaks (~0.4 mg m⁻³) around July and is lowest (~0.2 mg m⁻³) between October and January
395 (we also draw attention here to the work by Demarcq et al., 2020, for the Madagascar shelf).
396 South of 34°S, the emergence of the spring bloom is conspicuous between September and
397 December, with the southern part of the Madagascar Ridge showing earlier emergence than
398 farther south near the STF.

399

400 3.3 Ocean circulation (geostrophic currents)

401 3.3.1. Region view

402 **Fig. 5** shows the summer and winter climatologies (1993–2016) of the geostrophic
403 circulation in the greater vicinity of the Madagascar Ridge. The southern study boundary has
404 been extended to show the ARC. Eddies particularly dominant on the western side of the
405 Mozambique Channel, over the northern Madagascar Ridge (Halo et al., 2014; Vianello et al.,
406 2020), and along the boundary of the ARC are smoothed in these climatologies. The
407 dominant currents in the region, the EMC, the AC and the ARC, along with their
408 characteristics, are conspicuous year-round, with little seasonality in position and speed,

409 although the EMC tends on average to be stronger in winter than in summer (i.e. 60 vs. 70 cm
410 s^{-1}). Currents over the central and southern parts of the Ridge have on average low velocities
411 ($\sim 15 \text{ cm s}^{-1}$), with no coherence in the climatological mean direction, and they lack
412 seasonality.

413

414 3.3.2 Geostrophic currents over the Ridge (virtual moorings)

415 Details on the variability of the geostrophic currents along the Madagascar Ridge (shown in
416 **Fig. 5**) are now given in **Fig. 6**. These consist of 4-day vector time-series plots over a time-
417 span of 365 days (i.e. a vector every 4 days) for each of the VMs shown in **Fig. 2**. Four years
418 of data are plotted (2011–2014).

419

420 It is clear that geostrophic velocities generally decrease from north to south (i.e. VM 1 to VM
421 7). As seen by the steady southwesterly vectors in both annual maps (**Fig. 5**) and the 4-year
422 time-series (**Fig. 6**), VM 1 is firmly positioned in the S-EMC; there are only a few occasions
423 when this pattern deviates. Velocities generally range from 30 to 90 cm s^{-1} (see **Table 1** for
424 more detail), but can reach 118 cm s^{-1} (e.g. Day 161, 2013).

425

426 Velocities drop at VM 2 (MAD-Ridge), ranging between 10 and 70 cm s^{-1} , but on occasion
427 can reach 94 cm s^{-1} (e.g. Day 46, 2011). The direction of the current is far less constant and
428 with a strong eastward component. As demonstrated in Vianello et al., (2020), the MAD-
429 Ridge seamount is similarly in a zone of high mesoscale activity, with eddies occurring
430 93.8% of the time (1993–2016). Certainly, the passing of mesoscale eddies, with their
431 rotating currents, is evident in the 2011 time-series, but the more steady northeastward
432 current from mid-2012 to mid-2014 suggests the presence of SICC.

433

434 Velocities at VM 3 have a comparable range to those at VM 2 (i.e. 10–60 cm s^{-1}) and there is
435 little coherence in the current direction there. Currents can also on occasion reach 86 cm s^{-1}
436 (Day 41, 2011). The sequential rotation of vectors indicates that this position is still strongly
437 influenced by the passing EMC-generated eddies. These do not always correlate with the
438 currents for the same period at VM 2, especially between mid-2012 and mid-2014,
439 suggesting that the retroflection of the EMC is restricted to the area of VM 2.

440

441 Currents at VMs 4–7 all show similarly rotating vector patterns indicative of passing
442 mesoscale eddies (Quarty et al., 2006), albeit with decreasing velocities towards the Walters

443 Shoal (VM 6), i.e. $\sim 25 \text{ cm s}^{-1}$ reducing to $\sim 8 \text{ cm s}^{-1}$. As pointed out in **Fig. 3h**, Walters Shoal
444 is located in a region of very low EKE.

445

446 **Fig. 7** shows rose diagrams for the seven VMs using the full altimetry dataset from 1993–
447 2016 and provides convenient summaries of the mooring currents. The unidirectional
448 southwesterly current observed in the 4-year time-series at VM 1 is clear, but there is no
449 coherence in direction at the other 6 VMs. The decrease in velocities towards Walters Shoal
450 is also conspicuous, as is the slight increase farther south at VM 7. The dominant northeast
451 currents at VM 2 and VM 3 are evident.

452

453 *3.3.3 Monthly current climatologies over the Madagascar Ridge*

454 **Fig. 8** expands the knowledge gained from the 4-year records at the mooring sites (**Fig. 7**)
455 and provides a full monthly climatology (1993–2016) of the geostrophic currents over the
456 Madagascar Ridge (25–37°S). This serves to highlight gradients too, as shown for properties
457 in section 3.2 above. Note the scale change indicated by the black line in **Fig. 8**. The strong
458 southwestward currents shown in **Fig. 6** and **Fig. 7** north of the Mad-Ridge seamount are
459 seen in **Fig. 8** as being very persistent, signalling the dominance of the S-EMC year-round.
460 The northeast climatological currents seen between MAD-Ridge and 29°S (the black line),
461 would suggest the presence of the S-EMC retroflection, fitting the literature, but those in **Fig.**
462 **8** show a seasonality with stronger currents in summer (December–March) and weaker ones
463 in winter (May–July). A similar pattern is also observed south of Walters Shoal, but with a
464 longer period of weak currents during winter (March–August). This is interesting, because it
465 is the opposite pattern to that of wind and MLD shown in **Fig. 3**, which are both influenced
466 by the seasonal migration of the westerly wind belt.

467

468 As noted above, Walters Shoal is located in a region of particularly weak currents. North of
469 it, to 29°S (the black line), the great variability in currents highlighted above (**Fig. 7**), is
470 unambiguous with few obvious patterns, the exception possibly being just above 33°S
471 between September and December, when there appears to be a distinct southwesterly flow.

472

473 **4. Discussion**

474

475 *4.1 Gradients and surface layer properties at the seamounts*

476 As pointed out above, life on seamounts is structured by factors such as depth, horizontal and
477 vertical gradients of water column properties, latitudinal diversity gradient (LDG) and ocean
478 circulation. We therefore wanted to provide a regional view of surface wind as a driver, SST,
479 MLD and chl-*a* as key water column properties, and EKE and currents as drivers of seamount
480 processes and dispersion/connectivity. Focus was therefore on the three regionally prominent
481 shallow seamounts under investigation in the MADRidge Project, two on the Madagascar
482 Ridge, Walters Shoal and MAD-Ridge, and the other, La Pérouse, farther north and east of
483 Madagascar in the Madagascar Basin. The three span a distance of some 1500 km between 20
484 and 33°S. We summarise our results for wind, SST, MLD, chl-*a* and EKE in **Table 2**, to look
485 for similarities or differences between the three seamount environments. It is important to
486 remember that these results are climatological means. Combined with those in **Fig. 3** and **Fig.**
487 **4**, they show stark seasonally dependent differences along the Madagascar Ridge, and
488 moreover along the whole range of the study domain (20–33°S). Surface wind showed local
489 acceleration of the trade winds around the southern tip of Madagascar. This was also noticed
490 by Collins et al. (in prep.), who suggest enhanced coastal upwelling and productivity on the
491 shelf there. The productivity is seen in satellite observations being exported offshore in
492 filaments that extend onto the Ridge, reaching at times the MAD-Ridge seamount. This was
493 verified by Harris et al. (2020), who found substantial numbers of neritic fish larvae at MAD-
494 Ridge. We also observed the seasonal northward migration of the westerly wind belt (strong
495 winds) over the southern parts of the Ridge during the austral winter, but the strong winds do
496 not reach Walters Shoal.

497
498 SST showed strong gradients along the ridge between 26 and 40°S, ranging between 6 and
499 9°C throughout the year. This means that SST at Walters Shoal ranges from 19°C in August
500 to 24°C in February, and at MAD-Ridge from 23°C in August to 27°C in February, in each
501 case a 4–5°C difference. By comparison, SSTs at La Pérouse range from 25 to 28°C, a 1–2°C
502 difference from the situation at MAD-Ridge. The small difference is clearly helped by the
503 south-flowing warm water of the S-EMC, which passes La Pérouse in the form of the South
504 Equatorial Current, as seen by the configuration of the 23°C isotherm in **Fig. 3c** and **3d**.

505
506 MLD is uniform throughout the entire region in summer at ~40 m, but deepens over the
507 northern Ridge (at MAD-Ridge) in winter to ~60 m and then to ~100 m at Walters Shoal and
508 La Pérouse. These climatological mean depths do not correspond with cruise CTD data
509 collected in November 2009 (summer) by Read and Pollard (2017), who using temperature

510 and salinity vertical profiles for the Samper seamount at similar latitude (37°S, 52°E) but to
511 the east on the SWIR, observed the MLD around 130 m, but with large variance between 70
512 and 180 m on time-scales of 24 h as a consequence of internal tides. Comparison with Pollard
513 and Read (2017) revealed the Samper seamount to be in the centre of an intense (SSH ~140
514 cm) anticyclonic eddy, which deepens the thermocline (Huggett, 2014). This eddy probably
515 was spun-off the ARC. Given the eddy field over the Madagascar Ridge, large actual MLD
516 variance should be expected.

517

518 EKE is the energy associated with the turbulent part of fluid flow, and notably highlights
519 areas/regions with abundant mesoscale eddies. Apart from redistributing momentum and
520 physical tracers, mesoscale eddies, through their lateral stirring, mixing and vertical
521 advection of nutrients, substantially influence phytoplankton distributions, biogeochemical
522 cycles and pelagic ocean ecosystems (e.g. McGillicuddy et al., 1998; Garçon et al., 2001;
523 Yoder et al., 2010; Chelton et al., 2011a, b). Depending on their SSH, they invoke strong
524 rotational currents, as seen in **Fig. 6** of our analysis. Our results for EKE revealed the
525 northern part of the Ridge to be highly energetic in eddy activity, with the MAD-Ridge
526 seamount being on the southern edge of a high EKE corridor. A small seasonal signal was
527 detected in the corridor, with greater EKE between March and August. For the three
528 seamounts, EKE was therefore highest at MAD-Ridge ($414 \text{ cm}^2 \text{ s}^{-2}$ in winter), followed by La
529 Pérouse ($59 \text{ cm}^2 \text{ s}^{-2}$ in summer), then Walters Shoal ($28 \text{ cm}^2 \text{ s}^{-2}$). The eddy field drives the
530 current field, so speeds will similarly follow this trend (discussed further below).

531

532 Anticyclonic subtropical gyres in the oceans are regions of permanent downwelling and
533 consequently deep nutriclines, which limits algal development and subsequent biological and
534 biogeochemical processes (Tomczal and Godfrey, 1994). Morel et al. (2010), using satellite-
535 derived annual means over 10 years (1998–2007) showed chl-*a* concentrations for the South
536 Indian gyre to be $0.049 (\pm 0.006) \text{ mg m}^{-3}$, with a small but significant season cycle. Lowest
537 values were in December and highest values in August, two months after the winter solstice.
538 Low nutrient availability in the (sub)tropical oligotrophic ocean causes a dominance of
539 cyanobacteria such as *Synechococcus* and *Prochlorococcus* over picoeukaryotic
540 phytoplankton species (Li, 1994; Johnson et al., 2006). The domain of this study resides on
541 the western edge of the South Indian subtropical gyre (see Morel et al., 2010; their Fig. 1), so
542 we would expect chl-*a* mean values in our study to be a little higher than those given in
543 results for the gyre centre. Our chl-*a* maps in **Figs. 3i** and **3j** concur with this and similarly

544 highlight the oligotrophic nature of the region, with summer concentrations uniformly ~ 0.1
545 mg m^{-3} over the domain. However, this situation changes in winter, with the area east of the
546 Madagascar Ridge remaining low in chl-*a* (0.12 mg m^{-3}) and that west of the Ridge
547 approaching 0.3 mg m^{-3} . The longitudinal divide is aligned with the eastward base of the
548 Ridge, implying that Walters Shoal is located in the elevated chl-*a* zone. This situation is
549 shown in Table 2, with a climatological mean of 0.26 mg m^{-3} . MAD-Ridge, on the other
550 hand, with a winter value of 0.19 mg m^{-3} , is positioned right on the climatological divide.
551 Seasonal mean chl-*a* concentrations at La Pérouse remained particularly low at 0.07 mg m^{-3}
552 in summer and 0.12 mg m^{-3} in winter, confirming its location at the periphery of the gyre.
553 Demarcq et al. (2020) took this analysis further, and using a unique analysis based on a
554 satellite-derived chl-*a* enrichment index (EI) for the same domain, showed local enrichment
555 at Walters Shoal and at the nearby deeper WS-2 seamount (480 m from the surface). La
556 Pérouse and MAD-Ridge in their analysis exhibited sporadic or no measurable surface chl-*a*
557 maxima. However, it must be stressed that both this work and that of Demarcq et al. (2020)
558 are climatological analyses and eliminate chl-*a* signals generated by the shorter time-scales of
559 mesoscale dynamics, as mentioned by Vianello et al. (2020).

560

561 *4.2 Circulation (connectivity)*

562 As pointed out already, much is known about the boundary currents in the South West Indian
563 Ocean: the AC (Agulhas Current), the EMC (East Madagascar Current), and to a lesser extent
564 the ARC (Agulhas Return Current). These have attracted international attention owing to
565 their important role in the global thermohaline circulation (Rahmstorf, 2003). In determining
566 the characteristics, and particularly the volume transport, expensive projects have deployed
567 moorings across the Mozambique Channel (Ridderinkhof and de Ruijter, 2003), the AC (Beal
568 and Bryden, 1999; Morris et al., 2016) and more recently the EMC (Nauw et al., 2008). The
569 bottom of the S-EMC has also received attention, because it is one of the tributaries of the
570 AC. Those studies highlighted the dynamic nature of the region, with varying endpoint
571 configurations including retroflexion (Lutjeharms, 1988) and the generation of dipole eddies
572 (de Ruijter et al., 2004). Owing to the remoteness of the South Indian Ocean, studies on the
573 ARC have relied on remote sensing, in particular satellite-derived altimetry (Read and
574 Pollard, 1993; Lutjeharms and Ansorge, 2001; Quartly and Srokosz, 2003).

575

576 In contrast, little is known of the central region of the SWIO, which includes the central and
577 southern parts of the Madagascar Ridge. Read and Pollard (2017), for the only other

578 seamount study in the SWIO, used AVISO altimetry data to demonstrate that the area shows
579 slow mean westward flow between the southern tip of Madagascar and the ARC. Integrated
580 into this are slow (4.1 cm s^{-1}), west-propagating eddies. These control the currents at each of
581 the five seamounts on the SWIR and one on the Madagascar Ridge, a deep seamount called
582 Walter (1250 m), slightly northeast of Walters Shoal. The latter tended to experience eddies
583 coming from the northeast, producing currents with a mean speed of 18 cm s^{-1} and a
584 maximum of 27 cm s^{-1} (3-year time-series).

585

586 In the absence of *in situ* data, we too used satellite-derived altimetry data to estimate the
587 geostrophic current field in this SWIO. Our velocity vector maps highlighted the main
588 peripheral currents, the AC, the EMC and the ARC, with no obvious seasonal changes at this
589 level of investigation. And as with Read and Pollard (2017), they confirmed the central
590 region of the SWIO, including the central and southern parts of the Madagascar Ridge, as
591 having low current speeds. However, the use of virtual moorings based on 4-day altimetry
592 data along the Madagascar Ridge revealed far more detail of the circulation over the Ridge.
593 As highlighted in **Fig. 6**, the evolution of currents over the Ridge is seen with the passing of
594 eddies. Our analysis showed a strong gradient in current speed along the Ridge, with strong
595 (mean 58 cm s^{-1} ; max. 118 cm s^{-1}) unidirectional flow at the northern extreme, and much
596 slower, highly variable flow (mean 8.8 cm s^{-1} ; max. 24.5 cm s^{-1}) near Walters Shoal. At the
597 very southern reaches of the Ridge, currents strengthen a little. Those current regimes
598 (gradients) are clear in **Fig. 8**.

599

600 The implications of these results relate to connectivity in terms of the dispersion of biota
601 (larvae). In particular, we estimate that dispersion from MAD-Ridge, which is located
602 between the dominant southwesterly flow of the EMC and the eastward flow of the EMRC,
603 will be mostly zonal, with greater weight likely to eastward advection. Likewise, dispersion
604 from Walters Shoal, which has low velocity and a highly variable current regime, is likely to
605 be omnidirectional and, relative to MAD-Ridge, restricted in distance. We did not undertake
606 a full-depth analysis for La Pérouse, but given the low EKE ($58 \text{ cm}^2 \text{ s}^{-2}$), indicative of
607 moderate eddy intensity and frequency (and hence variable current direction), and its position
608 in the South Equatorial Current (SEC), with a mean velocity $\sim 17 \text{ m s}^{-1}$, dispersion is likely to
609 be omnidirectional but distance-restricted, but with an overall westward movement towards
610 Madagascar. Confidence in these extrapolations is provided by the comparison of our
611 geostrophic currents with actual *in situ* surface drift buoys (see Supplementary **Fig. S2**).

612 Indeed, these extrapolations are confirmed in Crochelet et al. (2020), who used an
613 individually based model (IBM) to investigate the connectivity of seamounts in the SWIO.
614 That model was driven by OSCAR data.

615

616 **5. Conclusions**

617

618 This study aimed to provide a SWIO regional view of surface wind as a driver (upwelling and
619 mixing), SST, MLD and chl-*a* as key water column properties, and EKE and currents as
620 drivers of seamount processes and dispersion/connectivity. We used satellite-derived mean
621 seasonal climatologies for these parameters with data spanning 16–22 years. EKE and current
622 speeds were high in the regional boundary currents (i.e. AC, S-EMC and ARC), but low over
623 the central parts of the region, notably the southern part of the Madagascar Ridge. Neither
624 EKE nor velocities show much seasonality. The strongest longitudinal gradients across the
625 region in winter were for wind, SST, MLD and chl-*a*.

626

627 We had particular focus on characterising the upper ocean environment near the three
628 prominent shallow seamounts, Walters Shoal, MAD-Ridge and La Pérouse. To this end, we
629 showed, relative to the other two seamounts, Walters Shoal to have the lowest mean wind
630 speed (6.7 m s^{-1} in winter), the lowest mean SST (18.4°C in winter), a deep mean MLD (82 m
631 in winter), the lowest mean current speed (9.8 cm s^{-1}) and the highest mean chl-*a* (0.26 mg m^{-3}
632 in winter). It also had the lowest mean EKE ($24.8 \text{ cm}^2 \text{ s}^{-2}$), indicative of low intensity, less
633 frequent eddies, so dispersion away from it would be limited.

634

635 La Pérouse, situated in the trade winds ($\sim 8 \text{ m s}^{-1}$), has the highest mean SST (27.7°C in
636 summer), surprisingly the deepest mean MLD (84 m during winter) and intermediate mean
637 current speeds ($\sim 18 \text{ cm s}^{-1}$). Mean chl-*a* levels were the lowest (0.07 mg m^{-3}) there, relative
638 to the other seamounts. Mean EKE ($59 \text{ cm}^2 \text{ s}^{-2}$) was twice that at Walters Shoal. Dispersion
639 from La Pérouse will therefore be greater than from Walters Shoal, but still limited.

640

641 MAD-Ridge in contrast is located in a much more energetic environment, with faster currents
642 (mean $\sim 38 \text{ cm s}^{-1}$), frequently passing eddies (high mean EKE of $\sim 400 \text{ cm}^2 \text{ s}^{-2}$) and high
643 SSTs (mean 25.8°C in summer) for its latitude, owing to the southward transport of tropical
644 warm water by the S-EMC. Dispersion and connectivity are therefore expected to be greatest
645 for MAD-Ridge.

646

647 The results given here provide, in our opinion, an appropriate backdrop for the detailed, ship-
648 based, physical and biological studies presented elsewhere in the MAD-Ridge special issue,
649 underpinning the enhanced knowledge gained on the pelagic ecosystems in the vicinity of
650 these shallow seamounts.

651

652 **Acknowledgements**

653

654 The work was supported financially and logistically by the Institut de Recherche pour le
655 Développement (IRD) and the Flotte Océanographique Française. Additional funding was
656 received from the Fonds Français pour l'Environnement Mondial (FFEM) on the Areas
657 Beyond National Jurisdiction (ABNJ) in the South West Indian Ocean. The MADRidge
658 Project was a joint venture between the IRD (France), UBO (Université de Bretagne
659 Occidentale) and the Nelson Mandela University (NMU) in South Africa, with support from
660 the Newton Fund and National Research Foundation (NRF) in the form of the UK-SA
661 Bilateral Research Chair in Ocean Science and Marine Food Security. The MADRidge
662 Project was carried out under the auspices of the Western Indian Ocean Upwelling Research
663 Initiative (WIOURI), which is part of the 2016–2025 International Indian Ocean Expedition
664 (IIOE-2) programme (Roberts, 2015).

665

666 **References**

667

- 668 Atlas, R., Hoffman, R., Ardizzone, J., Leidner, S., Jusem, J., Smith, D., Gombos, D., 2011. A
669 cross-calibrated, multiplatform ocean surface wind velocity product for meteorological
670 and oceanographic applications. *Bull. Am. Meteor. Soc.* 92, 157–174.
- 671 Beal, L., Bryden, H., 1999. The velocity and vorticity structure of the Agulhas Current at 32°
672 S. *J. Geophys. Res. Oceans* 104(C3), 5151–5176.
- 673 Braby, L., Backeberg, B., Anson, I., Roberts, M., Krug, M., Reason, C., 2016. Observed
674 eddy dissipation in the Agulhas Current. *Geophys. Res. Lett.* 43(15), 8143–8150.

- 675 Chelton, P.B., Gaube, P., Schlax, M.G., Early, J.J., Samelson, R.M., 2011b. The influence of
676 nonlinear mesoscale eddies on near-surface oceanic chlorophyll. *Science* 334(6054),
677 328–332. doi: 10.1126/science.1208897.
- 678 Chelton, D.G., Schlax, M.G., Samelson, R.M., 2011a. Global observations of nonlinear
679 mesoscale eddies. *Prog. Oceanogr.* 91(2), 167–216.
- 680 Clark, M.R., Vinnichenko, V.I., Gordon, J.D.M., Beck-Bulat, G.Z., Kukharev, N.N, Kakora,
681 A.F., 2007. Large-scale distant-water trawl fisheries on seamounts. In Pitcher, T.J.,
682 Morato, T., Hart, P.J.B., Clark, M.R., Haggan, N., Santos, R.S. (Eds), *Seamounts:
683 Ecology, Fisheries and Conservation 12*. Blackwell Publishing, Oxford, U.K, 361–399.
- 684 Clark, M.R., Schlacher, T.A., Rowden, A.A., Stocks, K.I., Consalvey, M., 2012). *Science
685 priorities for seamounts: research links to conservation and management*. *PLoS ONE*,
686 7(1), e29232. <https://doi.org/10.1371/journal.pone.0029232>.
- 687 Collins, M., Roberts, M.J., Ternon, J-F., Demarcq, H., Herbette, S., in preparation. Event-
688 scale (3–10 days) observations of upwelling on the southeast coast of Madagascar.
- 689 Crochelet, E., Barrier, N., Andrello, M., Marsac, F., Spadone, A., Lett, C., 2020. Connectivity
690 between seamounts and coastal ecosystems in the Southwestern Indian Ocean. *Deep-
691 Sea Res. II* (this issue).
- 692 de Boyer Montégut, C., Madec, G., Fischer, A., Lazar, A.S., Iudicone, D., 2004. Mixed layer
693 depth over the global ocean: an examination of profile data and a profile-based
694 climatology. *J. Geophys. Res.* 109(C12). <https://doi.org/10.1029/2004JC002378>.
- 695 Demarcq, H., Noyon, M., Roberts, M.J., 2020. Satellite observations of phytoplankton
696 enrichments around seamounts in the South West Indian Ocean, with a special focus on
697 the Walters Shoal. *Deep-Sea Res. II* (this issue).
- 698 de Ruijter, W., van Aken, H., Beier, E., Lutjeharms, J.R.E., Matano, R., Schouten, W., 2004.
699 Eddies and dipoles around South Madagascar: formation, pathways and large-scale
700 impact. *Deep-Sea Res. I* 51, 383–400.
- 701 Dilmahamad, A.F., Penven, P., Aguiar-González, B., Reason, C.J.C., Hermes, J.C., 2019. A
702 new definition of the South-East Madagascar bloom and analysis of its variability. *J.
703 Geophys. Res. Oceans*, 124. <https://doi.org/10.1029/2018JC014582>.
- 704 Evano, H., Bourjea, J., 2012. *Atlas de la pêche palangrière réunionnaise de l’océan Indien*.
705 RST –doi/2012-11. 245 pp.
- 706 Garçon, V., Oschlies, A., Doney, S., McGillicuddy, D., Waniek, J., 2001. The role of
707 mesoscale variability on plankton dynamics in the North Atlantic. *Deep-Sea Res. II* 48,
708 2199–2226.
- 709 Goslin, J., Segoufin, J., Schlich, R., Fisher, R.L., 1980. Submarine topography and shallow
710 structure of the Madagascar Ridge, western Indian Ocean. *GSA Bull.* 91(12), 741–753.
- 711 Halo, I., Penven, P., Backeberg, B., Ansorge, I., Shillington, F., Roman, R., 2014. Mesoscale
712 eddy variability in the southern extension of the East Madagascar Current: seasonal
713 cycle, energy conversion terms, and eddy mean properties. *J. Geophys. Res. Oceans*
714 119(10), 7324–7356.
- 715 Harris, P.T., MacMillan-Lawler, M., Rupp, J., Baker, E.K., 2014. Geomorphology of the
716 oceans. *Mar. Geol.* 352, 4–24.
- 717 Harris, S.A., Noyon, M., Marsac, F., Vianello, P., Roberts, M.J., 2020. Ichthyoplankton
718 assemblages at three shallow seamounts in the South West Indian Ocean. *Deep-Sea
719 Res. II* (this issue).
- 720 Huggett, J.A., 2014. Mesoscale distribution and community composition of zooplankton in
721 the Mozambique Channel. *Deep-Sea Res. II* 100, 119–135.
- 722 Johnson, Z.I., Zinser, E.R., Coe, A., McNulty, N.P., Woodward, E.M.S., Chisholm, S.W.,
723 2006. Niche partitioning among *Prochlorococcus* ecotypes along ocean-scale
724 environmental gradients, *Science* 311, 1737–1740.

- 725 Keating, B.H., Fryer, P., Batiza, R., Boehlert, G.W. (Eds), 1987. Seamounts, islands and
726 atolls. *Geophys. Monogr.* 43, 319–334.
- 727 Kitchingman, A., Lai, S., Morato, T., Pauly, D., 2007. How many seamounts are there and
728 where are they located? In Pitcher, T., Morato, T., Hart, P., Clark, M., Haggan, N.,
729 Santos, R., (eds) *Seamounts: Ecology, Fisheries and Conservation*. Fisheries and
730 Aquatic Resources Series, Blackwell, Oxford, 26–40.
- 731 Lavelle, J., Mohn, C., 2010. Motion, commotion, and biophysical connections at deep ocean
732 seamounts. *Oceanography* 23, 90–103.
- 733 Li, W.K.W., 1994. Primary production of prochlorophytes, cyanobacteria, and eukaryotic
734 ultraphytoplankton measurements from flowcytometric sorting. *Limnol. Oceanogr.* 39,
735 169–175.
- 736 Littler, M.M., Littler, D.S., Blair, S.M., Norris, J.N., 1986. Deep-water plant communities
737 from an uncharted seamount off San Salvador Island, Bahamas: distribution,
738 abundance, and primary productivity. *Deep-Sea Res.* I 33, 881–892.
- 739 Lutjeharms, J.R.E., 1988. Remote sensing corroboration of retroflexion of the East
740 Madagascar Current. *Deep-Sea Res.* A 35, 2045–2050.
- 741 Lutjeharms, J.R.E., 2006. *The Agulhas Current*. Springer, New York. 334 pp.
- 742 Lutjeharms, J.R.E., 2007. Three decades of research on the greater Agulhas Current. *O. Sci.*
743 *Europ. Geosci. Un.* 3(1), 129–147.
- 744 Lutjeharms, J.R.E., Anson, I., 2001. The Agulhas Return Current. *J. Mar. Sys.* 30, 115–138.
- 745 McGillicuddy, D.J., Robinson, A.R., Siegel, D.A., Jannasch, H.W., Johnson, R., Dicky, T.D.,
746 McNeil, J., Michaels, A.F., Knap, A.H., 1998. Influence of mesoscale eddies on new
747 production in the Sargasso Sea, *Nature*, 394, 263–266.
- 748 Morel, A., Claustre, H., Gentili, B., 2010. The most oligotrophic subtropical zone of the
749 global ocean: similarities and difference in terms of chlorophyll and yellow substance.
750 *Biogeosci.* 7, 3139–3151.
- 751 Morris, T., Hermes, J., Beal, L., du Plessis, M., Duncombe-Rae, C., Gulekana, M., Lamont,
752 T., Speich, S., Roberts, M., Anson, I.J., 2017. The importance of monitoring the
753 Greater Agulhas Current and its inter-ocean exchanges using large mooring arrays. *S.*
754 *Afr. J. Sci.* 113(7/8). <http://dx.doi.org/10.17159/sajs.2017/20160330>.
- 755 Nauw, J.J., van Aken, H.M., Webb, A., Lutjeharms, J.R.E., de Ruijter, W.P.M., 2008.
756 Observations of the southern East Madagascar Current and undercurrent and counter
757 current system. *J. Geophys. Res.* 113(C08006). <https://doi.org/10.1029/2007JC004639>
- 758 Palastanga, V., van Leeuwen, P.J., Schouten, M.W., de Ruijter, W.P.M., 2007. Flow structure
759 and variability in the subtropical Indian Ocean: instability of the South Indian Ocean
760 Countercurrent. *J. Geophys. Res. Oceans* 112(C1).
761 <https://doi.org/10.1029/2005JC003395>.
- 762 Parin, N.V., Mironov, A.N., Nesis, K.N. 1997. Biology of the Nazca and Sala y Gomez
763 submarine ridges, an outpost of the Indo-West Pacific fauna in the eastern Pacific
764 Ocean: composition and distribution of the fauna, its communities and history. *Adv.*
765 *Mar. Biol.*, 32, 145–242.
- 766 Pinet, P., Jaquemet, S., Phillips, R.A., Le Corre, M., 2012. Sex-specific foraging strategies
767 throughout the breeding season in a tropical, sexually monomorphic small petrel. *Anim.*
768 *Behav.* 83, 979–989. doi:/10.1012/j.anbehav.2012.01.19.
- 769 Pollard, R., Read, J., 2015. Circulation, stratification and seamounts in the south west Indian
770 Ocean. *Deep-Sea Res.* II 136, 36–43. doi:/10.1016/j.dsr2.2015.02.018.
- 771 Quartly, G., Buck, J., Srokosz, M., Coward, C., 2006. Eddies around Madagascar – the
772 retroflexion re-considered. *J. Mar. Syst.* 63(3–4), 115–129.
- 773 Quartly G.D., Srokosz M.A., 2003. Satellite observations of the Agulhas Current system.
774 *Phil. Trans. Appl. Math. Phys. Eng. Sci.* 361(1802), 51–56. doi:10.1098/rsta.2002.1107.

- 775 Rahmstorf, S., 2003. The current climate. *Nature*, 421, p. 699.
- 776 Read, J., Pollard, R., 1993. Structure and transport of the Antarctic Circumpolar Current and
777 Agulhas Return Current at 40°E. *J. Geophys. Res. Oceans* 98(C7), 12281–12295.
- 778 Read, J., Pollard, R., 2017. An introduction to the physical oceanography of six seamounts in
779 the southwest Indian Ocean. *Deep Sea Res. II* 136, 44–58.
- 780 Richer de Forges, B., Koslow, J., Poore, G., 2000. Diversity and endemism of the benthic
781 seamount fauna in the southwest Pacific. *Nature* 405, 944–947.
- 782 Ridderinkhof, H., de Ruijter, W.P.M., 2003. Moored current observations in the Mozambique
783 Channel. *Deep-Sea Res. II* 50, 1933–1955.
- 784 Ridderinkhof, W., Le Bars, D., von der Heydt, A.S., de Ruijter, W.P.M., 2013. Dipoles of the
785 South East Madagascar Current. *Geophys. Res. Lett.* 40(3), 558–562.
- 786 Roberts, M., 2015. The Western Indian Ocean Upwelling Research Initiative (WIOURI): a
787 Flagship IIOE2 Project. *CLIVAR Exchanges* No. 68, Vol. 19, No. 3, Nov 2015.
- 788 Roberts, M., Ternon, J-F., Morris, T., 2014. Interaction of dipole eddies with the western
789 slope of the Mozambique Channel. *Deep-Sea Research II* 100, 54–67.
790 <http://dx.doi.org/10.1016/j.dsr2.2013.10.016>.
- 791 Roberts, M.J., Ternon, J-F., Marsac, F., Noyon, M., Payne, A.I.L., 2020. The MADRidge
792 Project: Bio-Physical coupling around three shallow seamounts in the South West
793 Indian Ocean. *Deep-Sea Res. II* (this issue).
- 794 Rogers, A.D., 1994. The biology of seamounts. *Adv. Mar. Biol.* 30, 305–50.
- 795 Rogers, A.D., Alvheim, O., Bemanaja, E., Benivary, D., Boersch-Supan, P., Bornman, T.G.,
796 Cedras, R., Du Plessis, N., Gotheil, S., Høines, A., Kemp, K., Kristiansen, J., Letessier,
797 T., Mangar, V., Mazungula, N., Mørk, T., Pinet, P., Pollard, R., Read, J., Sonnekus, T.,
798 2017. Pelagic communities of the South West Indian Ocean seamounts: R/V *Dr Fridtjof*
799 *ansen* cruise 2009–410. *Deep-Sea Res. II* 136, 5–35.
- 800 Rubin, M.J., van Loon, H., 1953. Aspects of the circulation of the southern hemisphere. *J.*
801 *Meteorol.* 11, 68–76.
- 802 Siedler, G., Rouault, M., Biastoch, A., Backeberg, B., Reason, C.J.C., Lutjeharms, J.R.E.,
803 2009. Modes of the southern extension of the East Madagascar Current. *J. Geophys.*
804 *Res.* 114(C01005). doi:10.1029/2008JC004921
- 805 Siedler, G., Rouault, M., Lutjeharms, J.R.E., 2006. Structure and origin of the subtropical
806 South Indian Ocean Countercurrent. *Geophys. Res. Lett.* 33(24).
807 <https://doi.org/10.1029/2006GL027399>
- 808 Srokosz, M.A., Robinson, J., McGrain, H., Popova, E.E., Yool, A., 2015. Could the
809 Madagascar bloom be fertilized by Madagascan iron? *J. Geophys. Res. Oceans*, 120,
810 5790–5803, doi:10.1002/2015JC011075.
- 811 Stramma, L., Lutjeharms, J.R.E., 1997. The flow field of the subtropical gyre of the South
812 Indian Ocean. *J. Geophys. Res.* 102(C3), 5513–5530.
- 813 Thistle, D., 2003. The deep-seafloor: an overview. In Tyler, P.A. (Ed.). *Ecosystems of the*
814 *world* 28, *Ecosystems of the deep oceans*, Chapter 2. Elsevier Science, Amsterdam.
- 815 Tomczak, M., Godfrey, J.S. 1994. *Regional oceanography: an introduction*. Pergamon Press,
816 Oxford, 422 pp. ISBN 008-0410200.
- 817 Tyler, P., Bronsdon, S., Young, C., Rice, A., 1995. Ecology and gametogenic biology of the
818 genus *Umbellula* (Pennatulacea) in the North Atlantic. *Int. Rev. Gesamten Hydrobiol.*
819 *Hydrogr.* 80, 187–199.
- 820 Vianello, P., Herbette, S., Ternon, J-F., Demarcq, H., Roberts, M.J., 2020. Observation of a
821 mesoscale eddy dipole on the northern Madagascar Ridge: consequences for the
822 circulation and hydrography in the vicinity of a seamount. *Deep-Sea Res. II* (this issue).
- 823 Yoder, J., Doney, S., Siegel, D., Wilson, C., 2010. Study of marine ecosystems and
824 biogeochemistry now and in the future: examples of the unique contributions from

825 space. *Oceanography* 23(4), 104–117. Retrieved 6 June 2020, from
826 www.jstor.org/stable/24860866.

827

828 **Figure legends**

829

830 Fig. 1. (a) The South Western Indian Ocean subgyre forms the background circulation to the
831 SWIO region (blue box). This is portrayed by the baroclinic volume flux field over the upper
832 1000 m (after Stramma and Lutjeharms, 1997). Transport volumes are in $10^6 \text{ m}^3 \text{ s}^{-1}$. (b)
833 Schematic showing the major oceanographic features of the SWIO (adapted after Lutjeharms,
834 2006). The shaded bathymetry south of Madagascar identifies the Madagascar Ridge.

835

836 Fig. 2. (a) Bathymetry of the Madagascar Ridge (Gebco 2014 product) with two longitudinal
837 transects (white and black). The seven black dots indicate the positions of the virtual
838 moorings (VMs) referred to in text. (b) Vertical cross-sections of the bathymetry along these
839 transects. The dashed line is along the white transect. Grey shading is along the black
840 mooring line. Crosses along the top depict the positions of the virtual moorings (numbered),
841 and serve as grid points to extract altimetry data.

842

843 Fig. 3. Summer and winter wind field and ocean properties in the greater region of the
844 Madagascar Ridge: (a) and (b) Surface winds (1993–2015), (c) and (d) SST (1998–2014), (e)
845 and (f) MLD (1985–2009), (g) and (h) EKE (1993–2016), (i) and (j) Chl-*a* (1998–2016). The
846 two horizontal black lines indicate the latitudes of the MAD-Ridge seamount (27.5°S) and
847 Walters Shoal (33.25°S), and the black diamonds indicate the seven virtual moorings along
848 the Madagascar Ridge. For convenience, the 20°C (blue), 23°C (pink) and 25°C (red)
849 isotherms are shown in (c) and (d). All maps have a GEBCO 2014 bathymetry overlay.

850

851 Fig. 4. Climatological Hovmoller plots detailing gradients of water properties along the
852 Madagascar Ridge (averaged in the area between 43–48°E and 26–40°S, shown by the box in
853 the bottom right plot): (a) surface winds, (b) SST, (c) MLD, (d) EKE, (e) chl-*a*.

854

855 Fig. 5. Climatology of the surface circulation in the vicinity of the Madagascar Ridge in (a)
856 summer and (b) winter. GEBCO 2014 bathymetry is shown with black contours.

857

858 Fig. 6. Four-day vector time-series of geostrophic currents between 2011 and 2014 for the
859 seven virtual mooring sites (numbered) along the Madagascar Ridge, as shown on Fig. 2. The
860 scale is given at the bottom right.

861

862 Fig. 7. Rose diagrams of geostrophic currents between 1993 and 2016 at virtual moorings
863 (VMs) 1–7.

864

865 Fig. 8. Monthly mean climatology of geostrophic currents along the Madagascar Ridge for
866 the period 1993–2016. Blue lines indicate the position of the MAD-Ridge seamount (27.5°S,
867 top) and Walters Shoal (33.25°S, bottom). The black line indicates a change of scale for
868 current strength, indicated in the key to the right.

869

870 **Supplementary material**

871

872 Fig. S1. Comparison of absolute geostrophic velocity (Panel A) and OSCAR-derived near-
873 surface velocity (Panel B), using rose diagrams for data between 1993 and 2016 for each

874 virtual mooring (VM) 1–7. The colour scale is the same in (A) and (B), but differs for the
875 frequency scale between sites.

876

877 Fig. S2. Validation of satellite-derived geostrophic currents near Walters Shoal using SVP
878 drifters. See Section 2.3 for the altimetry data used. Colour tracks represent 24-day
879 trajectories of 6 SVP drifters released on 30 June 2014 in the vicinity of the seamount during
880 an ACEP cruise (on RV *Algoa*). Black dots show the simulated geostrophic progressive
881 vector trajectory. There is good agreement between the *in situ* data and the satellite-derived
882 geostrophic circulation, albeit the latter having an average velocity that is lower by some 8
883 cm s^{-1} . The difference is attributable to Ekman drift.

884

Journal Pre-proof

885 **Table 1.** Geostrophic current statistics for the virtual moorings (VM 1–7) over a 4-year period.
 886

| Mooring | 2011 | | 2012 | | 2013 | | 2014 | |
|---------|------------------------------|-------------------------------|------------------------------|-------------------------------|------------------------------|-------------------------------|------------------------------|-------------------------------|
| | Max (cm s ⁻¹) | Mean (cm s ⁻¹) | Max (cm s ⁻¹) | Mean (cm s ⁻¹) | Max (cm s ⁻¹) | Mean (cm s ⁻¹) | Max (cm s ⁻¹) | Mean (cm s ⁻¹) |
| VM 1 | 104.69 | 60.53 ± 22.88 | 107.61 | 59.85 ± 20.68 | 118.13 | 59.37 ± 25.58 | 114.4 | 50.35 ± 26.66 |
| VM 2 | 94.26 | 38.76 ± 18.48 | 73.38 | 33.43 ± 17.48 | 63.55 | 27.43 ± 11.6 | 74.75 | 32.67 ± 17 |
| VM 3 | 86.18 | 40.88 ± 22.06 | 67.07 | 24.61 ± 15.77 | 73.59 | 22.61 ± 15.02 | 79.69 | 31.34 ± 17.92 |
| VM 4 | 61.19 | 24.25 ± 13.56 | 59.33 | 31.06 ± 11.13 | 66.66 | 21.64 ± 14.3 | 47.4 | 14.72 ± 9.08 |
| VM 5 | 32.21 | 13.44 ± 6.51 | 69.96 | 20.14 ± 17.9 | 20.05 | 10.68 ± 4.81 | 32.42 | 12.37 ± 6.48 |
| VM 6 | 20.57 | 9.43 ± 4.64 | 24.46 | 7.8 ± 4.84 | 17.37 | 8.06 ± 3.36 | 21.3 | 9.78 ± 5.27 |
| VM 7 | 35.89 | 17.87 ± 6.93 | 40.48 | 11.35 ± 7.77 | 31.84 | 12.49 ± 7.27 | 27.48 | 10.58 ± 5.35 |

887

888

889

890

891 **Table 2.** Grid point extraction and summary of parameters from the climatological maps shown in
 892 Fig. 3 and Fig. 5 at the three seamounts for summer (DJF) and winter (JJA). Values are means \pm
 893 standard deviation.

| Variable | MAD-Ridge | | Walters Shoal | | La Pérouse | |
|--------------------------------------|---------------------|---------------------|-------------------|-------------------|-------------------|-------------------|
| | Summer | Winter | Summer | Winter | Summer | Winter |
| Wind Speed (m s^{-1}) | 8.41 \pm 1.02 | 8.53 \pm 1.12 | 6.71 \pm 0.97 | 8.03 \pm 1.04 | 6.36 \pm 0.8 | 8.12 \pm 0.97 |
| SST ($^{\circ}\text{C}$) | 25.79 \pm 0.72 | 22.99 \pm 0.96 | 21.84 \pm 0.64 | 18.4 \pm 0.53 | 27.7 \pm 0.81 | 24.78 \pm 0.92 |
| MLD (m) | 29.81 \pm 9.37 | 54.25 \pm 14.11 | 26.13 \pm 7.08 | 82.09 \pm 21.24 | 29.26 \pm 7.07 | 84.09 \pm 14.86 |
| EKE ($\text{cm}^2 \text{s}^{-2}$) | 397.61 \pm 223.33 | 413.78 \pm 231.33 | 28.33 \pm 13.94 | 24.83 \pm 12.12 | 58.97 \pm 24.36 | 56.92 \pm 22.13 |
| Chl- α (mg m^{-3}) | 0.14 \pm 0.04 | 0.19 \pm 0.02 | 0.14 \pm 0.03 | 0.26 \pm 0.04 | 0.07 \pm 0.02 | 0.12 \pm 0.02 |
| G. Velocity (cm s^{-1}) | 35.64 \pm 19.4 | 37.92 \pm 19.78 | 9.73 \pm 5.22 | 9.39 \pm 5.24 | 18.04 \pm 9.55 | 16.82 \pm 9.92 |

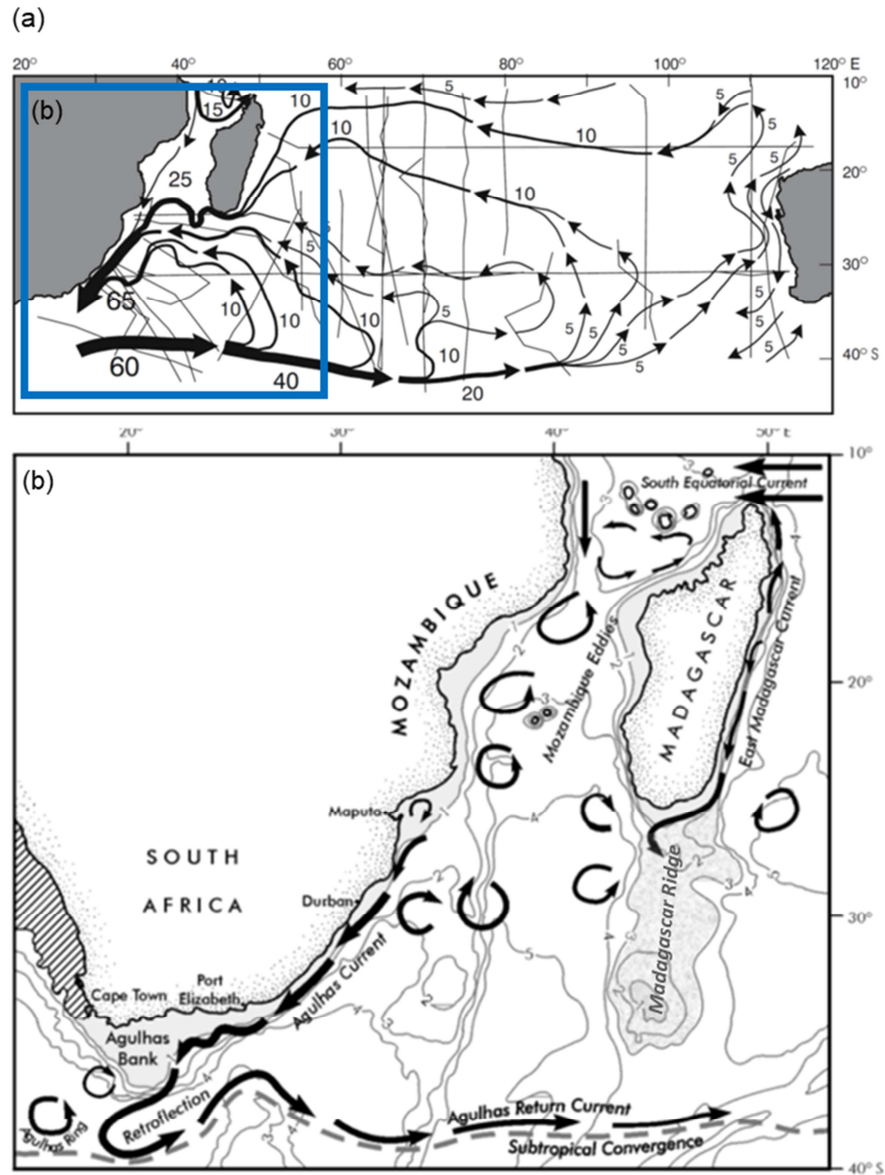


Fig. 1.

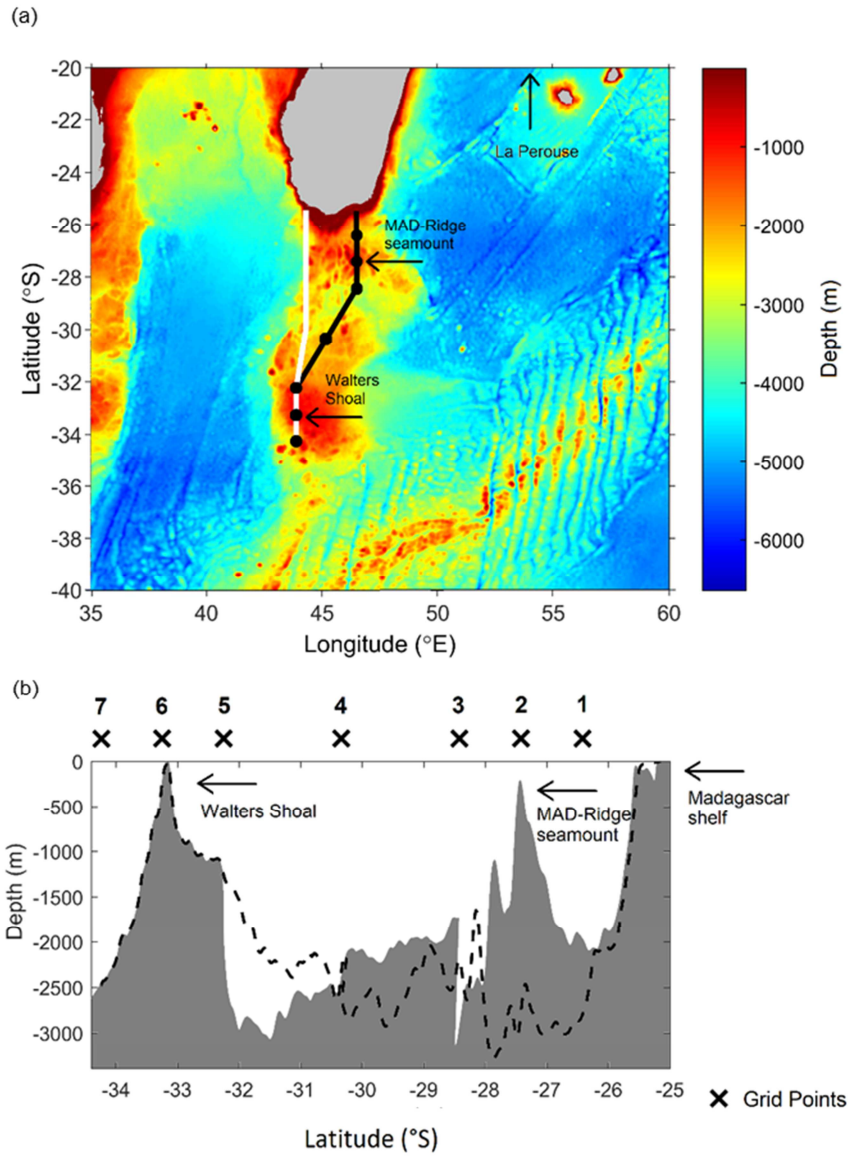


Fig. 2.

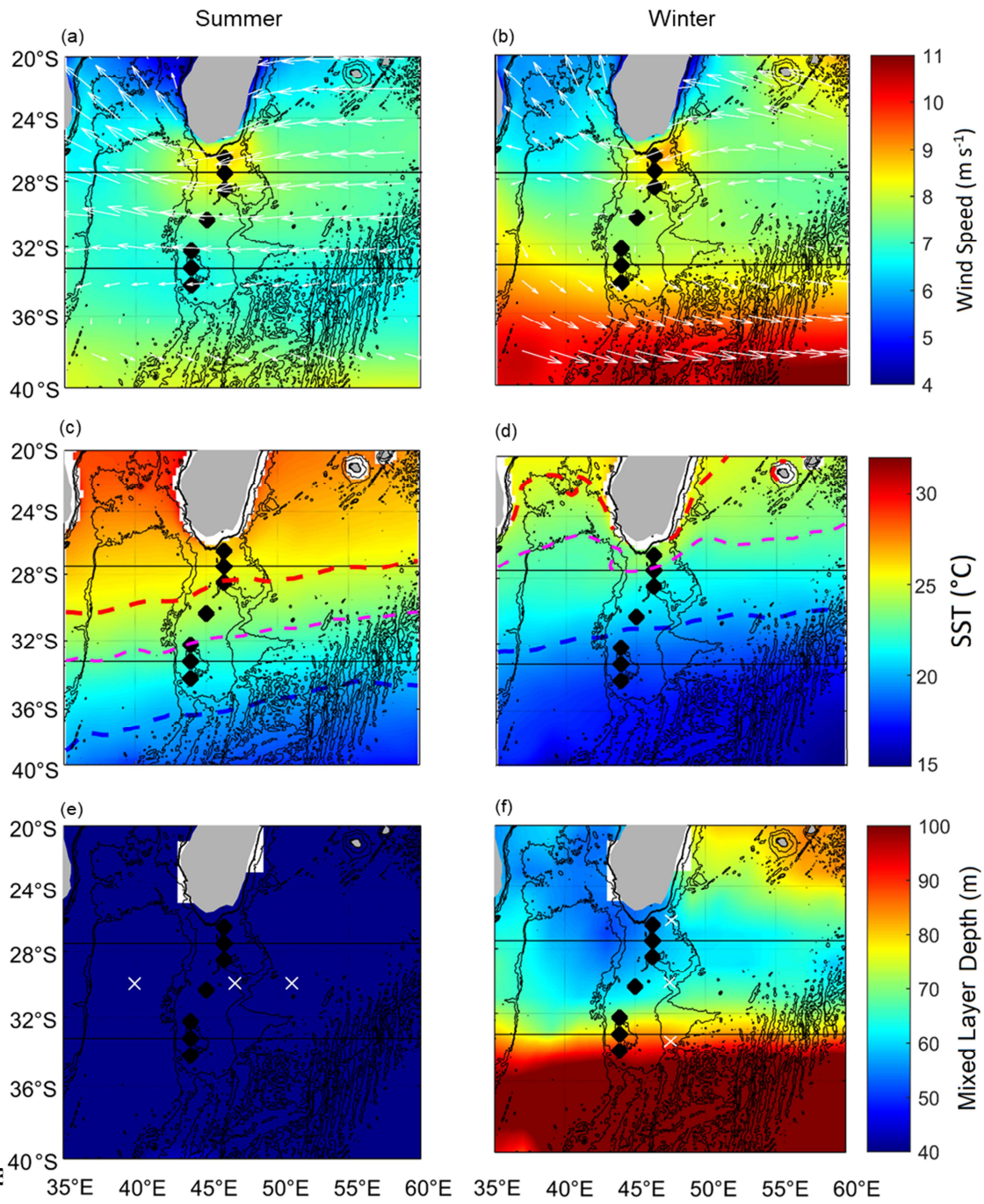


Fig. 3

Journal Pre-proof

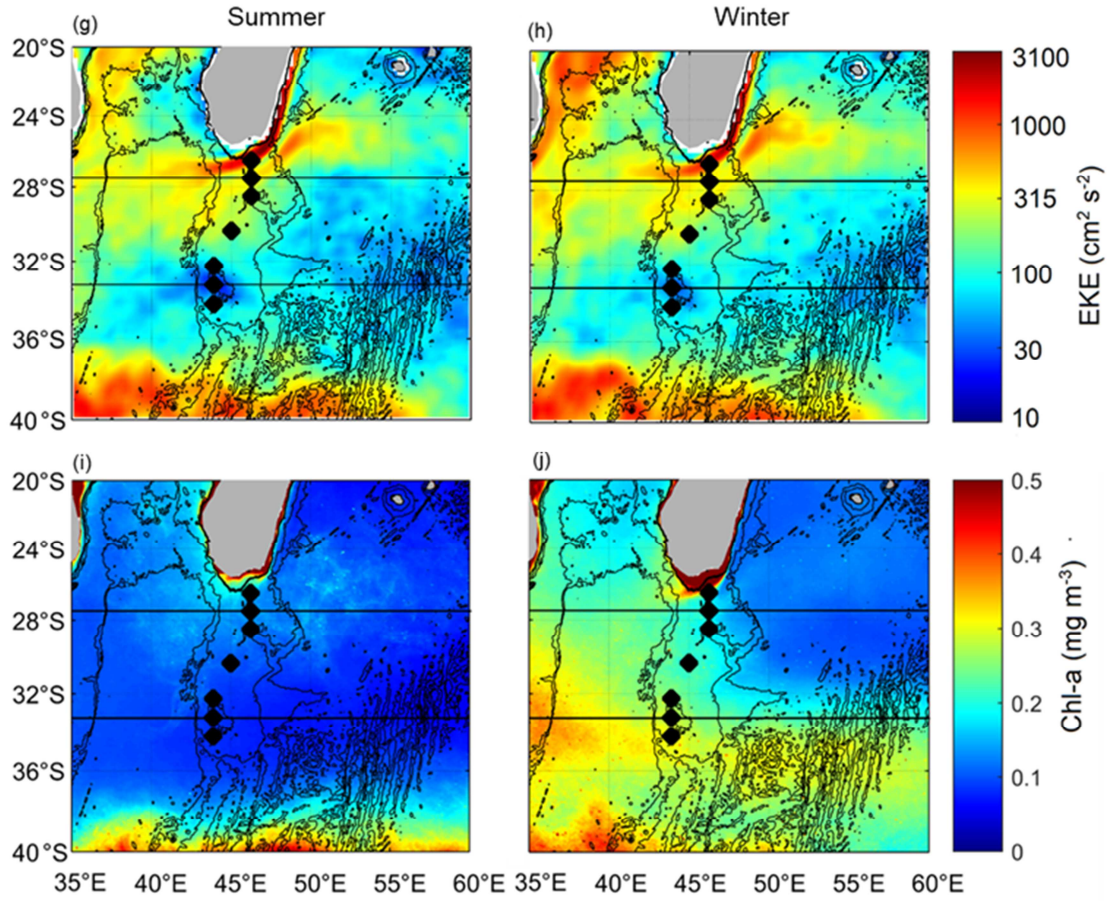


Fig. 3. (Continued)

Journal Pre-proof

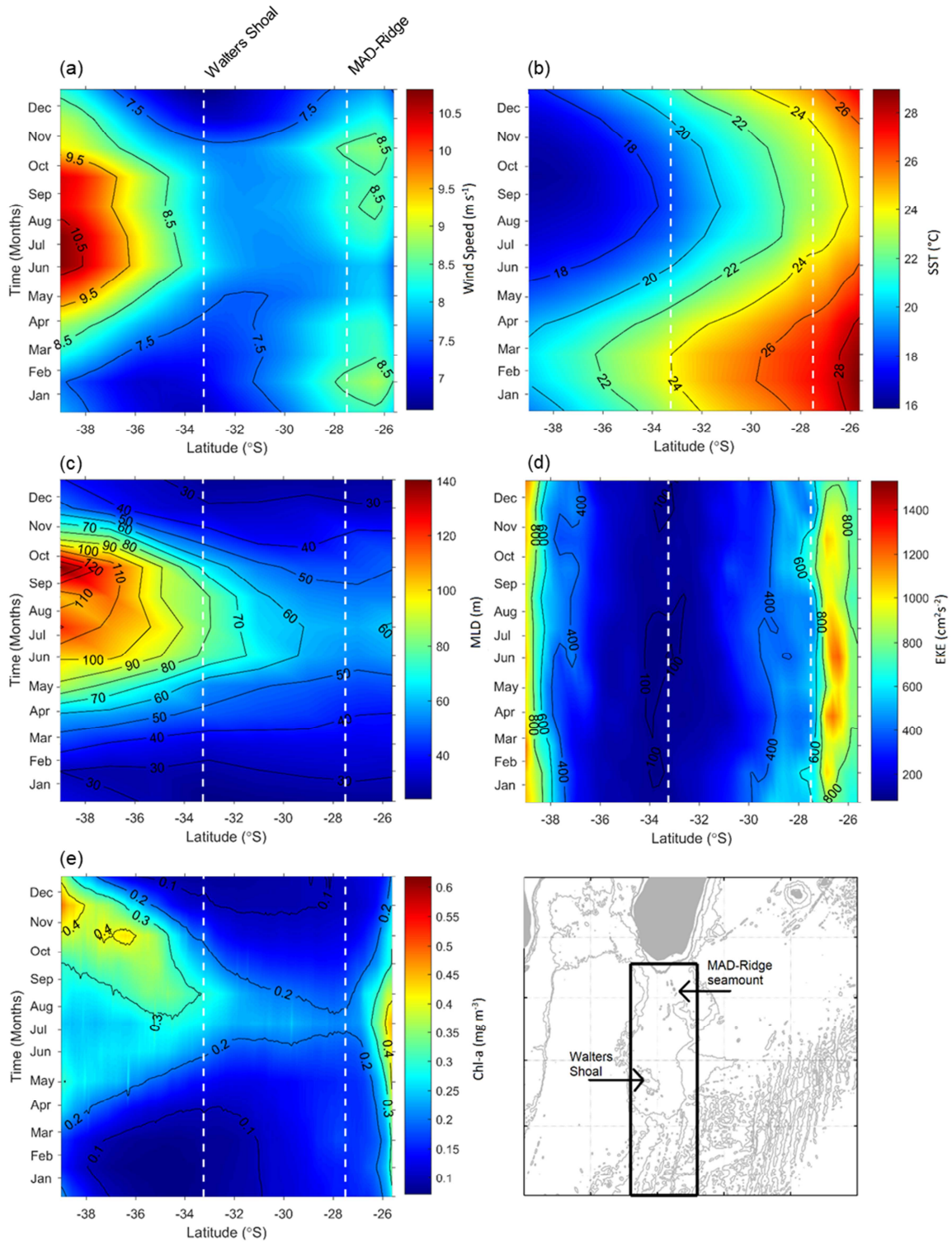


Fig. 4.

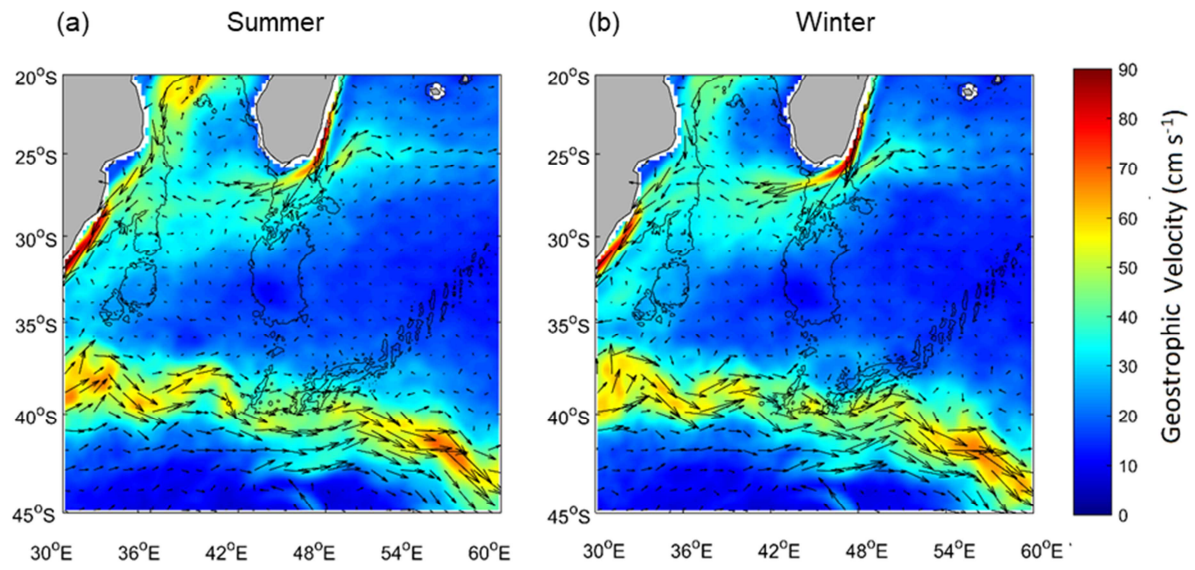


Fig. 5.

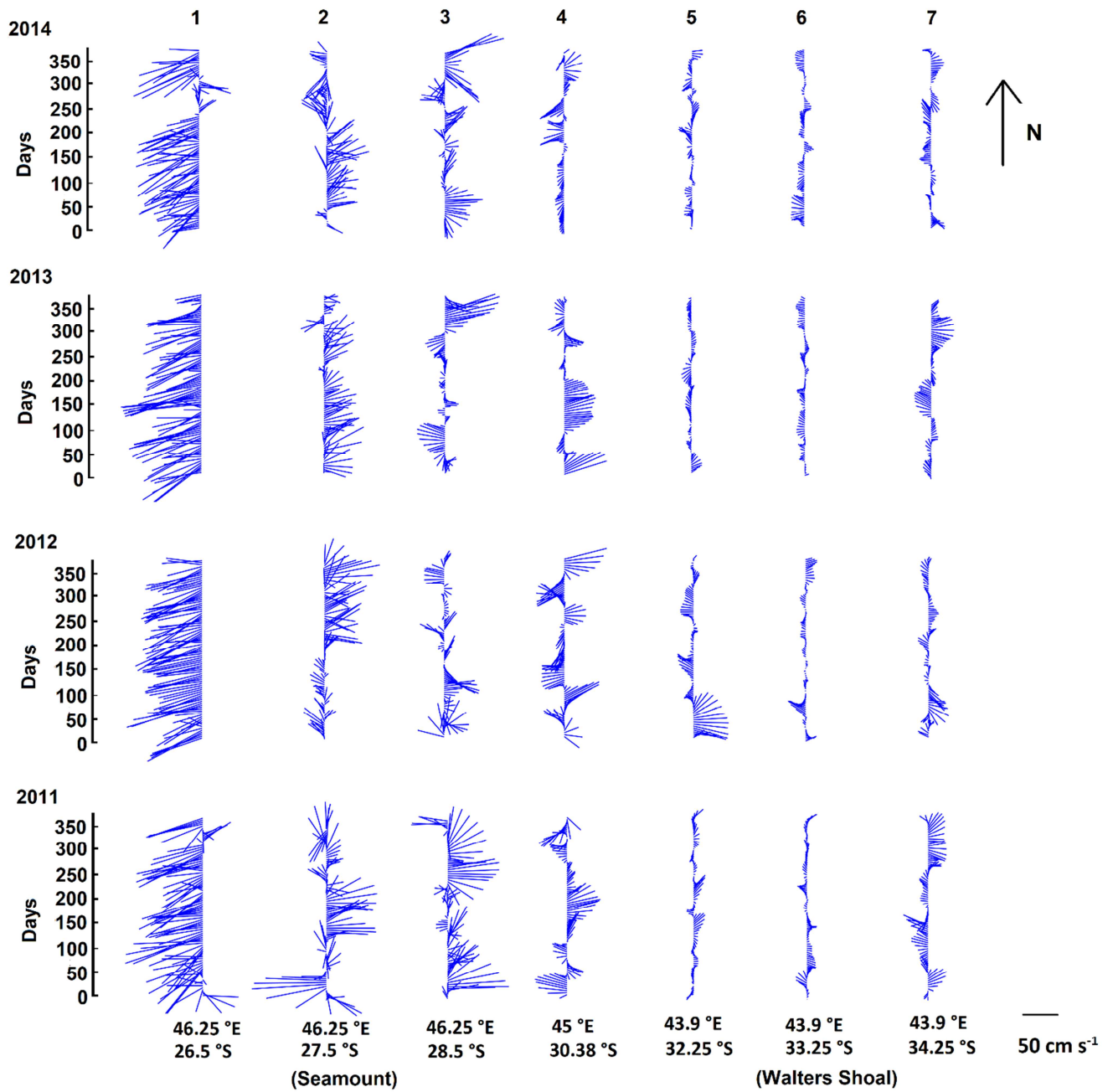


Fig. 6.

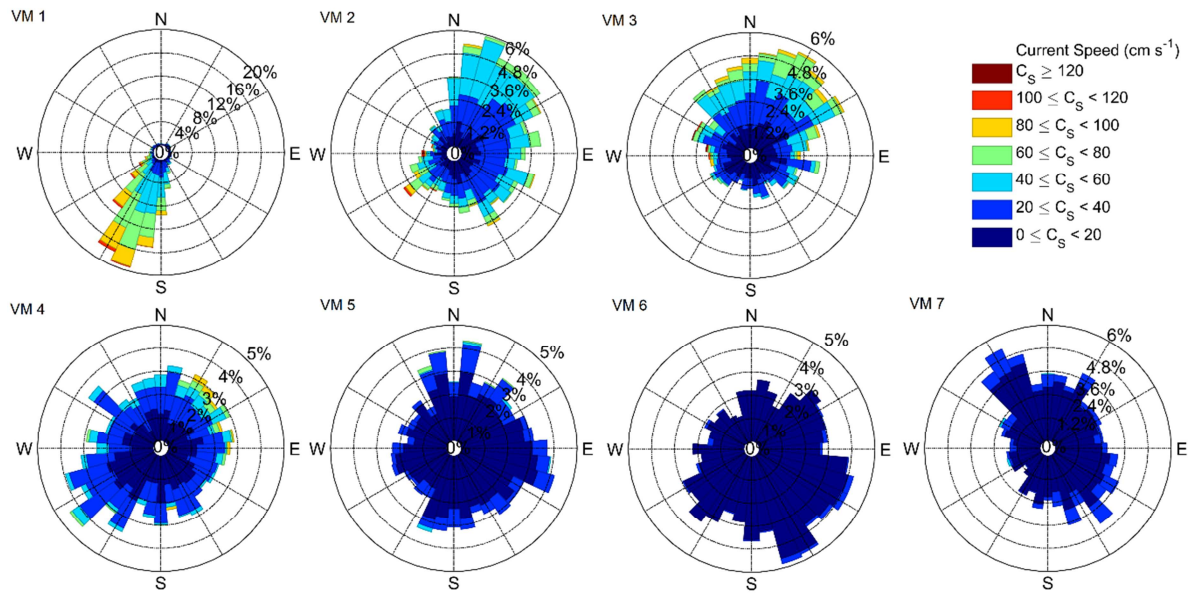


Fig. 7.

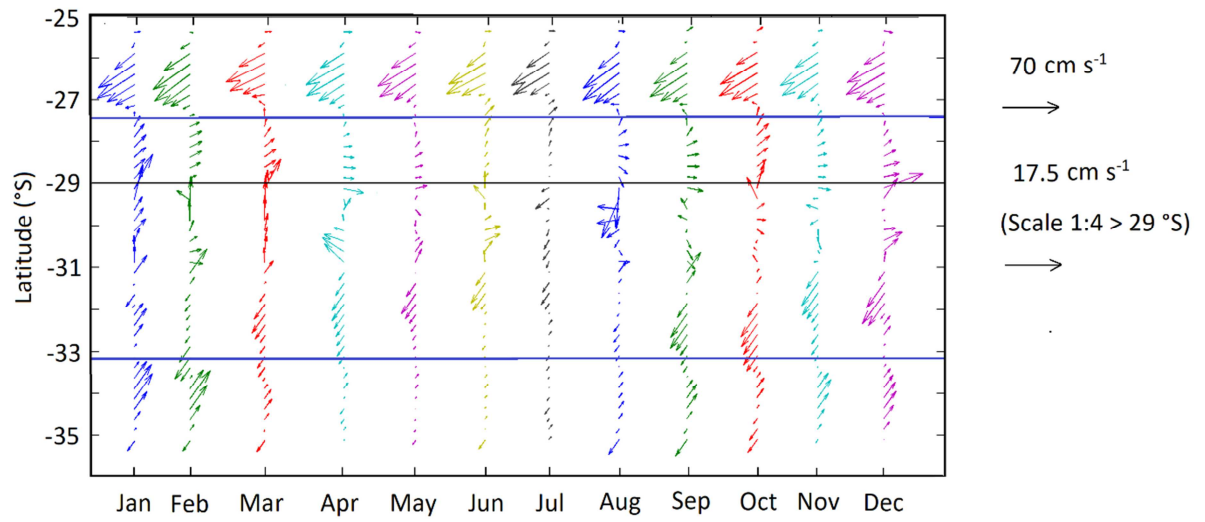
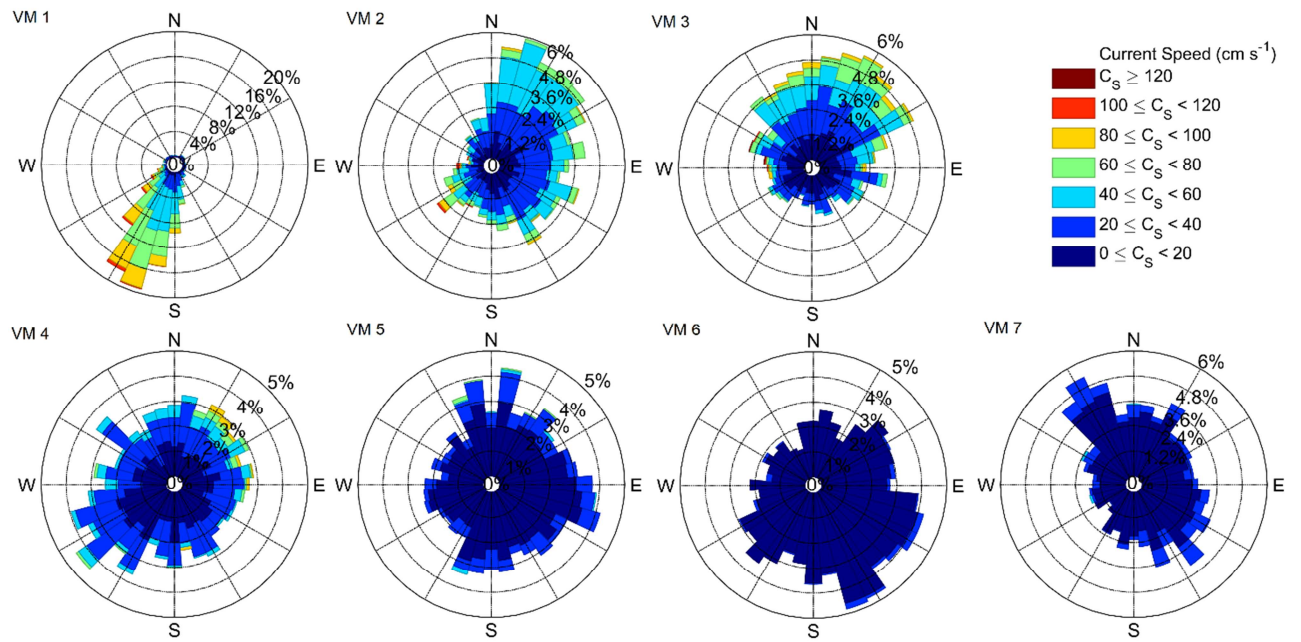


Fig. 8.

Journal Pre-proof

Panel (A)



Panel (B)

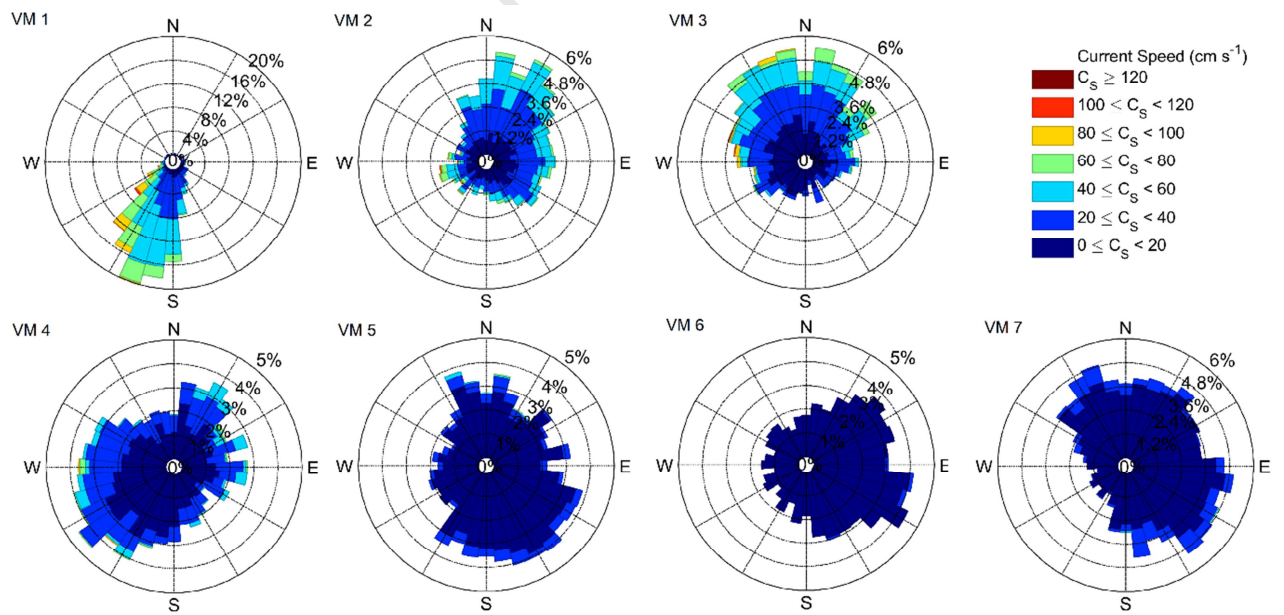


Fig. S1.

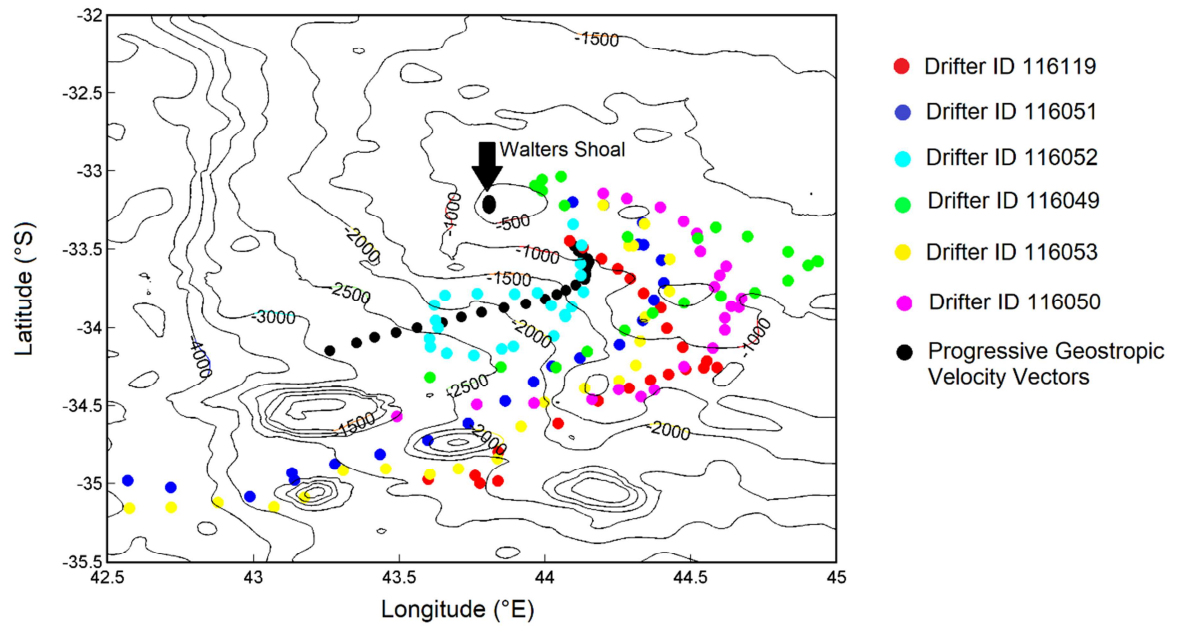


Fig. S2.

Author's Declaration of Interest

Regarding the submission of the research manuscript untitled:

Ocean currents and environmental gradients in the vicinity of the Madagascar Ridge in the Southwest Indian Ocean

We wish to confirm that there are no known conflicts of interest associated with this publication and there has been no significant financial support for this work that could have influenced its outcome.

We confirm that the manuscript has been read and approved by all named authors and that there are no other persons who satisfied the criteria for authorship but are not listed. We further confirm that the order of authors listed in the manuscript has been approved by all of us.

We confirm that we have given due consideration to the protection of intellectual property associated with this work and that there are no impediments to publication, including the timing of publication, with respect to intellectual property. In so doing we confirm that we have followed the regulations of our institutions concerning intellectual property.

We confirm that the work described has not been published previously, that it is not under consideration for publication elsewhere, that its publication is approved by all authors and that, if accepted, it will not be published elsewhere in the same form, in English or in any other language, including electronically without the written consent of the copyright-holder.

We further confirm that any aspect of the work covered in this manuscript that has involved experimental animals has been conducted with the ethical approval of all relevant bodies.

We understand that the Corresponding Author is the sole contact for the Editorial process (including Editorial Manager and direct communications with the office). She is responsible for communicating with the other authors about progress, submissions of revisions and final approval of proofs. We confirm that we have provided a current, correct email address which is accessible by the Corresponding Author and which has been configured to accept email from patrick.vianello2@gmail.com

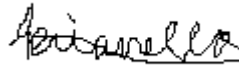
Signed by all authors as follows:

LIST OF AUTHORS

Patrick Vianello (corresponding author)

Date 04/12/2019

Signature



Jean-François Ternon

Date 04/12/2019

Signature



Hervé Demarcq

Date 04/12/2019

Signature

Steven Herbette

Date 04/12/2019

Signature

Michael Roberts

Date 03/12/2019

Signature

Journal Pre-proof